Journal of Low Temperature Physics, Vol. 76, Nos. 3/4, 1989

NMR and Axial Magnetic Field Textures in Stationary and Rotating Superfluid ^{3}He-B

P. J. Hakonen, M. Krusius, M. M. Salomaa, R. H. Salmelin, and J. T. Simola

Low Temperature Laboratory, Helsinki University of Technology, Espoo, Finland

and

A. D. Gongadze, G. E. Vachnadze, and G. A. Kharadze

Institute of Physics, Georgian Academy of Sciences, Tbilisi, USSR

(Received February 10, 1989)

We have performed NMR measurements on the flare-out texture of superfluid ^{3}He-B in a cylindrical container of 5 mm diameter in axial magnetic fields of 28.4 and 56.9 mT. The transverse cw NMR spectra have been analyzed both with respect to their overall shape and the spin-wave absorption peaks close to the Larmor frequency. Our analysis of the stationary state spectra, based on texture computations, yields the longitudinal resonance frequency $\nu_L(T)$, the magnetic healing length $\xi_H(T)$, and the dipolar length $\xi_D(T)$, which we report for pressures below 29 bar. A lattice of quantized vortex lines appears in the rotating state, and two additional textural free energy terms have to be included in the analysis. One of the terms is linear in the applied magnetic field and arises from the spontaneous magnetization of the vortex cores. The second term is quadratic in magnetic field; it is generated both by the superflow field $v_s(r)$ about the vortex core and the difference in the induced magnetizations of the vortex-core and the bulk superfluids. The rotational orienting effects have been studied for rotation speeds Ω up to 2 rad/sec.

1. INTRODUCTION

Since the discovery[1] of the superfluid phases of liquid ^{3}He in 1972, a large number of experimental and theoretical investigations have been carried out on these coherent states of matter at ultralow temperatures. Up to 1981, all efforts, with the exception of some early theoretical work, had concentrated on the properties of superfluid ^{3}He in stationary sample containers. The early eighties were marked by new achievements in this

0022-2291/89/0800-0225$06.00/0

respect when two rotating ultralow-temperature cryostats were put into operation.[2,3] It then became possible to study superfluid ^{3}He in rotation and, over a relatively short period of time, a considerable amount of new information was accumulated on many unique and mostly unexpected rotational flow phenomena in these anisotropic superfluids.[4–10]

Superfluids in general are characterized by spontaneously broken gauge symmetry and therefore display a peculiar equilibrium structure in a state of rotational flow. The simplest type of rotational motion, corresponding to the "solid body" distribution of the velocity field, is incompatible with the constraints imposed by the topology of the order parameter space. It is for this reason that in superfluid ^{4}He, for instance, the uniformity of the order parameter distribution is broken in rotational flow conditions by the formation of a lattice of singular quantized vortex lines with a density n_v proportional to the angular velocity Ω of rotation. The superfluid ^{3}He phases are described with order parameters possessing a much more complicated structure and therefore display a correspondingly larger variety of rotational flow phenomena. The ^{3}He-A order parameter is invariant under a combined gauge-orbit transformation, which opens up the possibility for the vorticity to be continuously distributed over one unit cell in a lattice of quantized vortex lines, i.e., ^{3}He-A is capable of mimicking solid body rotation even in the absence of vortex lines with a singular core. For ^{3}He-B the situation is quite different; its symmetry group contains as a continuous subgroup the combined rotation of the spin and orbital coordinates but does not contain the gauge group. As a result, both the gauge symmetry and the relative spin-orbit symmetry are found to be broken. Thus ^{3}He-B is characterized by phase and by spin-orbit coherence, which in rotation at equilibrium leads to the formation of a lattice of singular quantized vortex lines, similarly as in superfluid ^{4}He. However, in ^{3}He-B a large number of different structures for the singular core become possible.

The quantized vortices of ^{3}He-B are singular in the sense that inside the vortex core, with a cross-sectional size of the order of the superfluid coherence length, the order parameter changes continuously from one of the many core state distributions to its asymptotic B-phase form well outside the core.[11] This does not mean that the core would mainly consist of a normal state fraction as is the case for the ^{4}He vortex where the order parameter goes to zero at the center of the core. In superfluid ^{3}He the cores have macroscopic extensions, and the order parameter includes in its most general form nine complex components. It thus becomes possible to match the B-phase order parameter smoothly to some nonzero, intracore structure with a minimum loss of condensation energy. In fact, it can be shown that

in the core region, depending on pressure and temperature various order parameter distributions become possible solutions, and that a first-order phase transition between two structures with different discrete symmetries is a plausible explanation[12,13] for the hysteretic discontinuity which is observed in the NMR measurements in the rotating state.[4,14]

An applied magnetic field removes the isotropy of the superfluid energy gap and causes the B-liquid to exhibit orbital anisotropy. Via the interplay of different anisotropic interactions caused by both the intrinsic ^{3}He-B properties and by external influences, a spatially varying "texture" in the alignment of the anisotropy axis is formed. For instance, in a stationary cylindrical container in an axial magnetic field, the stable equilibrium texture is a "flare-out" configuration (see Fig. 1). It results from the combined action of the magnetic field and the container walls in the presence of the gradient energy which resists rapid changes in the order parameter orientation. In addition, in the rotating state, the kinetic energy of the superflow circulating around the vortex core contains a term which depends on the relative orientation of the superfluid velocity and the axis of orbital anisotropy. This contribution among others, which is proportional to n_v, thus changes the equilibrium texture as a function of the rotation velocity Ω. The misalignment of the ansotropy axis from the external field direction causes the NMR frequency to shift from the Larmor value, which in turn provides a highly sensitive means for studying the order parameter texture experimentally. These considerations form the basis for our measurements

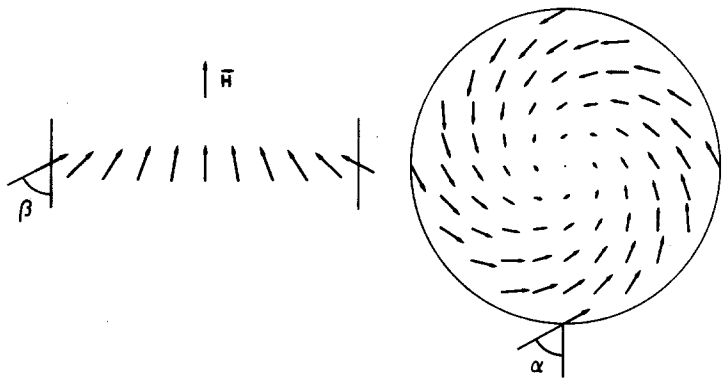

Fig. 1. Schematic illustration of the axially symmetric flare-out texture in a cylindrical container. A transverse cut through the cylinder is shown on the right-hand side, the arrows denote the projections of $\hat{\mathbf{n}}$ in the transverse xy-plane. A longitudinal cut along the cylinder axis is shown on the left, the arrows illustrate the radial distribution of β. The orientation of $\hat{\mathbf{n}}$ is specified by means of the azimuthal angle α and the polar angle β.

and their interpretation. The results illustrate a rich variety of textural phenomena and the profound influence from the quantized vortex lines in the rotating state.

In Sec. 2 we shall first briefly recount some of the theoretical ingredients for describing the anisotropic properties of the magnetized B-liquid, the flare-out texture in a cylindrical container and its distinctive NMR signature. In Sec. 3 we present the results from the stationary state measurements along with the method for extracting the values of the different textural parameters. Section 4 deals with the rotating state measurements which allow two additional textural free energy contributions to be determined. These arise from the influence of the rectilinear quantized vortices and yield quantitative data on the vortex structure. The main results from these measurements have been briefly reported in different contexts; here we have attempted to provide a more uniform presentation of the NMR properties and the original experimental data. The stationary state NMR properties were actually known more than a decade ago (see Refs. 15–17), but the present measurements have added some new details. Perhaps more important is the extended conceptual understanding which is gained from including rotation as a further dimension to the externally controllable parameter space.

2. THEORETICAL PRELIMINARIES

2.1. Textural Energies

In contrast to the A-phase, which exhibits intrinsic orbital and magnetic anisotropy, ^{3}He-B is isotropic in the absence of external influences. However, in an applied magnetic field, it acquires orbital anisotropy via spin-orbit coherence and a direct coupling of the magnetic field to the spin degrees of freedom. To study the consequences from the induced orbital anisotropy, we have to refer to the structure of the order parameter in the presence of a magnetic field $\mathbf{H}$. For the magnetized ^{3}He-B, the components of the order parameter matrix are given by

$$A_{\mu i} = \Delta_{\mu\nu} R_{\nu i}(\hat{\mathbf{n}}, \Theta) e^{i\phi} \tag{1}$$

where ϕ is the phase angle of the superfluid condensate and $\Delta_{\mu\nu}$ is the uniaxial gap matrix

$$\Delta_{\mu\nu} = \Delta_{\parallel} h_\mu h_\nu + \Delta_\perp (\delta_{\mu\nu} - h_\mu h_\nu) \tag{2}$$

The unit vector $\hat{\mathbf{h}} = \mathbf{H}/H$ specifies the magnetic anisotropy axis, while $\Delta_\perp$ and $\Delta_\parallel$ are the energy gaps perpendicular and parallel to the anisotropy axis ($\Delta_\perp = \Delta_\parallel = \Delta$ when $H = 0$ and $T < T_c$). $R_{\nu i}(\hat{\mathbf{n}}, \Theta)$ are the elements of a

rotation matrix for rotating the spin and orbital coordinates relative to each other by an angle Θ about an axis oriented along the unit vector $\hat{\mathbf{n}}$, i.e.,

$$R_{ij}(\hat{\mathbf{n}}, \Theta) = \delta_{ij} - (1 - \cos\Theta)(\delta_{ij} - n_i n_j) + \varepsilon_{ijk} n_k \sin\Theta \tag{3}$$

The rotation becomes fully specified in the presence of the spin-orbit coupling, i.e., the magnetic dipole-dipole interaction which is given by the free energy expression

$$F_D = \tfrac{1}{5} g_D (A^*_{\mu\mu} A_{ii} + A^*_{\mu i} A_{i\mu}) \tag{4}$$

Here the magnitude of the dipolar coupling parameter g_D is best characterized by its relation to the angular frequency $\omega_L(P, T) = 2\pi\nu_L$ of longitudinal NMR (see Fig. 10)

$$g_D = \chi_B \omega_L^2 / (3\gamma^2 \Delta_B^2)$$

The B-phase longitudinal NMR frequency ω_L in turn determines the scale of the frequency shifts in conventional transverse NMR (cf. Eq. (31)). The transverse NMR shift is the principal experimental observable in the present measurements. $\chi_B(T)$ is the B-phase susceptibility, $\Delta_B(T)$ the zero-field energy gap, and γ the gyromagnetic ratio of the ^{3}He nuclear magnetic moment. Returning back to Eqs. (1) and (4), we note the remarkable property of ^{3}He-B that F_D obtains its minimum value when the rotation angle Θ is fixed at $\Theta_0 = \arccos(-1/4)$. Furthermore, in the relatively low-magnetic fields of the present experiment, the order parameter field in Eq. (1) displays a texture which is formed by a slow variation in the local orientation of the rotation axis $\hat{\mathbf{n}}$.

To determine the equilibrium distribution of the directrix $\hat{\mathbf{n}}$, one has to consider the orientation dependent energy contributions to the orbital anisotropy energy. The most important contribution is the magnetic anisotropy energy of the magnetically distorted B-liquid, which orients the stationary bulk liquid far from any surfaces and is given by the orientation dependent part of the spin-orbit coupling in Eq. (4). The tensor $A^*_{\mu i} A_{\mu j}$ can be expressed in terms of an orbital anisotropy axis which is oriented along the unit vector $\hat{\mathbf{l}}_B$ such that

$$\hat{\mathbf{l}}_B = \hat{\mathbf{h}}\hat{\mathbf{R}}(\hat{\mathbf{n}}, \Theta) = \cos\Theta\,\hat{\mathbf{h}} + (1 - \cos\Theta)(\hat{\mathbf{h}} \cdot \hat{\mathbf{n}})\hat{\mathbf{n}} + \sin\Theta\,\hat{\mathbf{h}} \times \hat{\mathbf{n}} \tag{5}$$

Then

$$A^*_{\mu i} A_{\mu j} = \Delta_\parallel^2 l_{Bi} l_{Bj} + \Delta_\perp^2 (\delta_{ij} - l_{Bi} l_{Bj}) \tag{6}$$

With these notations we obtain from Eq. (4) a free energy contribution

$$F_{DH} = -\frac{4}{15} \chi_B \left(\frac{\omega_L}{\gamma}\right)^2 \left[\delta_B \left(\frac{3}{2} + 2\cos\Theta\right) \hat{\mathbf{h}} \cdot \hat{\mathbf{l}}_B - \frac{1}{2} \delta_B^2 (\hat{\mathbf{h}} \cdot \hat{\mathbf{l}}_B)^2 \right] \tag{7}$$

which depends on the relative orientation of $\hat{\mathbf{l}}_B$ and $\hat{\mathbf{h}}$. Here $\delta_B = (\Delta_\perp - \Delta_\parallel)/\Delta_\perp$ is the gap anisotropy parameter which is of the order $\delta_B \simeq (H/H_c)^2$ when $H \ll H_c$. H_c represents the field for which the magnetic anisotropy energy $(\chi_N - \chi_B)H_c^2/2$ equals the condensation energy for Cooper pairing. With $\cos\Theta_0 = -1/4$, one can finally write the magnetic orientational free energy in the form

$$\delta F_{DH} = -aH^2(\hat{\mathbf{n}} \cdot \hat{\mathbf{h}})^2 + \text{const} \tag{8}$$

where the orientational magnetic anisotropy constant a is given by

$$a = \frac{1}{3}\chi_B \left(\frac{\omega_L}{\gamma H_c}\right)^2$$

Although the orientational free energies are minute, experimentally, the textures become observable by virtue of the high degree of correlation in the superfluid phase and the high resolution of the NMR method.

The magnetic orientational energy in Eq. (8) favors parallel or antiparallel alignment of $\hat{\mathbf{n}}$ along $\hat{\mathbf{h}}$. In addition one has to take into account the influence from the walls of the container and the bending of the $\hat{\mathbf{n}}$-orientation from that at the walls towards the alignment along the external field direction far inside the bulk liquid. The equilibrium texture corresponds to the configuration for which the magnetic and bending energies integrated over the volume are minimized, subject to the boundary condition that the orientation at the walls is fixed by a separate minimization of the surface energy. The resulting textures have a characteristic length scale, the magnetic healing length ξ_H, which is of the order of 1 mm in typical NMR conditions. The large value of ξ_H is a prominent property of the B-liquid, a manifestation of the inherent stiffness of the $\hat{\mathbf{n}}$-field by way of the large size of the gradient energy as compared to the bulk liquid orientational energies. The B-phase textures in the stationary state were first comprehensively discussed in Ref. 15, which also describes the flare-out texture for the cylindrical geometry in an axial magnetic field. In the present context, the main emphasis will be centered on the textures of the rotating state and, specifically, on the methods of extracting new information on the structure of isolated vortex lines via their influence on the large-scale, global texture. Therefore, in the remainder of this subsection, we shall limit the discussion on one particular example of the orientational effects from the presence of vortices and, with respect to the more general textural features and principles, we refer to the existing literature.[15-17] However, we want to point out that rotation is the most effective means of erasing defects from textures and, therefore, we have used the present stationary state NMR spectra, which have turned out to be exceptionally clean and ordered, for extracting values for the various textural parameters like $\omega_L(P, T)$ and $\xi_H(P, T)$.

Let us next focus on the orientational influence from the superflow circulating an isolated vortex line with a velocity field $\mathbf{v}_s = (\hbar/2m)\nabla\phi$ in the presence of an anisotropic superfluid density $\rho^{(s)}$.[18] The hydrodynamic expression for the energy density in the supercurrent is given by

$$F_{\text{flow}} = \tfrac{1}{2}\rho_{ij}^{(s)} v_{si} v_{sj} \tag{9}$$

For this we need to consider the anisotropic part of the kinetic energy of the magnetized ^{3}He-B. Note first that the induced orbital anisotropy leads to a corresponding anisotropy in the quasiparticle excitation spectrum

$$E_{\mathbf{p}} = [\varepsilon^2(\mathbf{p}) + |\Delta(\mathbf{p})|^2]^{1/2} \tag{10}$$

where $\varepsilon(\mathbf{p}) = \mathbf{p}^2/(2m) - \varepsilon_F$ and $\boldsymbol{\Delta}(p)$ is the anisotropic energy gap. For a p-wave state, $\Delta(\mathbf{p})$ is linear with $\mathbf{p}$ such that $\Delta_\mu = A_{\mu i}\hat{\mathbf{p}}_i$ (since $|\mathbf{p}| \simeq p_F$) and

$$|\Delta(\hat{\mathbf{p}})|^2 = \Delta_\perp^2[1 - \delta_B(2 - \delta_B)(\hat{\mathbf{p}} \cdot \hat{\mathbf{l}}_B)] \tag{11}$$

Consequently, since $\hat{\mathbf{l}}_B$ acts as an anisotropy axis of the gap, the density of the normal component of the magnetized B-liquid has to be expressed by the uniaxial tensor

$$\rho_{ij}^{(n)} = \rho_\parallel^{(n)} l_{Bi} l_{Bj} + \rho_\perp^{(n)}(\delta_{ij} - l_{Bi} l_{Bj}) \tag{12}$$

where, however, the density anisotropy $\delta\rho_{\text{an}} = \rho_\perp^{(n)} - \rho_\parallel^{(n)}$ remains small since $\delta_B \ll 1$. A standard weak coupling calculation with the inclusion of the Fermi-liquid corrections gives for the density anisotropy the result

$$\delta\rho_{\text{an}}/\rho = -\frac{2}{5}\delta_B \frac{(1 + F_1^s/3)Z(T)}{[1 + F_1^s Y(T)/3]^2} \tag{13}$$

Here $Y(T)$ is the Yosida function while the related function $Z(T)$ is given by

$$Z(T) = (\Delta_B/2T)^2 \int_{-\infty}^{+\infty} \frac{\tanh(E_p^o/2T)}{\cosh^2(E_p^o/2T)} \frac{d\varepsilon(\mathbf{p})}{E_p^o} \tag{14}$$

E_p^o is the isotropic excitation spectrum $E_p^o = (\varepsilon^2(\mathbf{p}) + \Delta_B^2)^{1/2}$. Note that $Y(T_c) = 1$ and drops monotonically to zero as the temperature decreases while $Z(T)$ has a maximum at $T \simeq 0.7\ T_c$ and vanishes at both $T = T_c$ and $T = 0$.

Writing

$$\rho_{ij}^{(s)} = \rho\delta_{ij} - \rho_{ij}^{(n)} = (\rho - \rho_\perp^{(n)})\delta_{ij} + \delta\rho_{\text{an}} l_{Bi} l_{Bj} \tag{15}$$

we arrive at the following expression for the anisotropic contribution to the

kinetic energy of superflow:

$$\delta F_{\text{flow}} = \delta F_{vH} = \frac{1}{2}\,\delta\rho_{\text{an}}(\mathbf{v}_s \cdot \hat{\mathbf{l}}_B)^2$$

$$= -\frac{2}{15}\,\chi_B \left(\frac{\omega_L}{\gamma v_D}\right)^2 \delta_B (\mathbf{v}_s \cdot \hat{\mathbf{l}}_B)^2 \tag{16}$$

Here, to facilitate the comparison with the orientational contribution from magnetic anisotropy in Eq. (8), we have introduced the dipole velocity v_D, defined by the relation

$$v_D^{-2} = \frac{3}{2}\,\frac{\rho\gamma^2}{\chi_B \omega_L^2}\,\frac{(1+F_1^s/3)Z(T)}{[1+F_1^s Y(T)/3]^2} \tag{17}$$

This Eq. (17) reduces for $T \to T_c$ to

$$v_D = (g_D/\rho_s)^{1/2}$$

In Eq. (16) we have also used an alternative notation δF_{vH} to emphasize that this contribution to the anisotropy energy results from the combined effect of the hydrodynamic flow and the magnetic field.

Combining the kinetic term δF_{vH} in Eq. (16) with the spin-orbit contribution δF_{DH} in Eq. (8), we obtain expression (18) for the anisotropy energy density of the magnetized ^{3}He-B in the presence of superfluid counterflow

$$F_{\text{an}} = \delta F_{DH} + \delta F_{vH} = -\frac{4}{15}\,\chi_B \delta_B \left(\frac{\omega_L}{\gamma}\right)^2 \left[\hat{\mathbf{h}} \cdot \hat{\mathbf{l}}_B + \frac{1}{2}\left(\frac{\mathbf{v}_s \cdot \hat{\mathbf{l}}_B}{v_D}\right)^2\right] \tag{18}$$

It should be kept in mind that when $\mathbf{v}_s$ is large, we must also add the dipolar contribution $F_{DV} \propto \mathbf{v}_s \cdot \ddot{\mathbf{R}} \cdot \mathbf{v}_s$ to the energy density in Eq. (18), but its role is insignificant at the present level of magnetic fields when $H \gg H_D$. The dipolar field $H_D \simeq [g_D \Delta^2/(\chi_N - \chi_B)]^{1/2}$, which characterizes the magnitude of the dipole interaction with respect to the susceptibility anisotropy, is only $\sim$3 mT.

Next we analyze the role of the anisotropy energy in Eq. (18) in the formation of the $\hat{\mathbf{n}}$-field texture of rotating ^{3}He-B. Initially immediately after turning on the rotation, the counterflow of the superfluid and the normal components must be most strongly felt, when the normal liquid has already become involved in the solid-body motion while the superfluid is still at rest (as in ^{4}He-II, the establishing of an equilibrium lattice of quantized vortices requires a macroscopic time, of order 10 sec.[4]). In this initial nonequilibrium situation $\mathbf{v}_s = -\boldsymbol{\Omega} \times \mathbf{r}$ (since Eq. (18) should be applied to a rotating system of coordinates) and if $\Omega r > v_D$ in the main part of the volume, then the counterflow must have a substantial effect on the $\hat{\mathbf{n}}$-field texture.[19] As the superfluid component gradually becomes involved in the

rotation and the vortex lattice is formed, the effect of the counterflow is weakened and, once an equilibrium state with $\langle \nabla \times \mathbf{v}_s \rangle = 2\boldsymbol{\Omega}$ has been set up, then the counterflow will become concentrated only around the vortices. Consider now the situation where the radius of the Wigner–Seitz cell of the vortex lattice $r_v = [\hbar/(4m\Omega)]^{1/2}$ is much smaller than ξ_H, the usual experimental condition, then we can average the second term in Eq. (18) over the vortex lattice. Since the superflow $\mathbf{v}_s$, which circulates around the vortex core, is perpendicular to $\boldsymbol{\Omega}$, it follows that

$$\langle (\mathbf{v}_s \hat{\mathbf{l}}_B)^2 \rangle = \tfrac{1}{2}\langle v_s^2 \rangle [1 - (\hat{\boldsymbol{\Omega}} \cdot \hat{\mathbf{l}}_B)^2] \tag{19}$$

Thus we find that to within a constant term

$$F_{\text{an}} = -aH^2[(\hat{\mathbf{n}} \cdot \hat{\mathbf{h}})^2 - \tfrac{2}{5}\lambda_f(\hat{\mathbf{h}}\hat{\mathbf{R}}(\hat{\mathbf{n}}, \Theta_0)\hat{\boldsymbol{\Omega}})^2] \tag{20}$$

where the dimensionless parameter $\lambda_f = \langle v_s^2 \rangle/(2v_D^2)$ characterizes the strength of the global coupling of the system of vortices to the $\hat{\mathbf{n}}$-field.[18]

Noting now that for the system of quantized vortices

$$\langle v_s^2 \rangle = n_v \int_{\xi_c}^{r_v} \left(\frac{\hbar}{2mr}\right)^2 2\pi r \, dr = \frac{\hbar}{m} \Omega \ln(r_v/\xi_c) \tag{21}$$

where ξ_c and r_v are the radii of the singular vortex core and the Wigner–Seitz cell of the vortex lattice, respectively. Using Eq. (17) for the dipole velocity v_D, we then arrive at the following estimate for $\lambda_f = \lambda_f(P, T)$:

$$\lambda_f = \frac{3}{2} \frac{\hbar\rho}{2m\chi_B} \left(\frac{\gamma}{\omega_L}\right)^2 \Omega \frac{(1 + F_1^s(P)/3)Z(T)}{[1 + F_1^s(P)Y(T)/3]^2} \ln(r_v/\xi_c) \tag{22}$$

In Fig. 2 the temperature dependence of λ_f is shown at various pressures. The important features are the continuous increase of λ_f with decreasing pressure while the temperature dependence is nonmonotonic: λ_f starts from a finite value near T_c (neglecting the divergence of ξ_c at T_c), passes through a maximum at about $0.5T_c$ and then rapidly falls to zero with decreasing temperature. The last property is clearly a consequence from the Galilean invariance, as a result of which the orbital anisotropy of the superfluid must disappear as $T \to 0$ (recall that according to Eq. (16) $\delta F_{vH} \propto \delta\rho_{\text{an}}$). In Sec. 4 we shall see that these features are prominently reflected also in the experiments. However, due to the approximate nature of Eq. (22) and the arbitrary definition of the core radius ξ_c, a comparison with experiment can only be made on a qualitative level.

Equation (22) accounts for the global orienting effect from the superflow which circulates around each individual vortex line with the cutoffs in the integral fixed at ξ_c and r_v. However, the region inside the core ($r < \xi_c$), to where the B-phase does not extend, also gives a contribution to the anisotropy energy. To estimate the corresponding core parameter λ_c, which

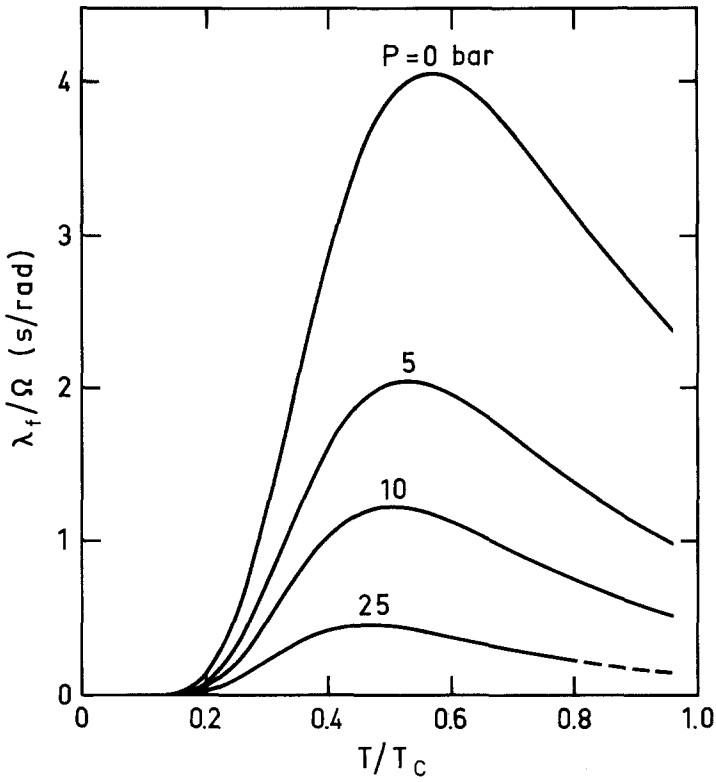

Fig. 2. Temperature dependence of the orientational free energy parameter λ_f, i.e., the magnitude of the textural influence of the superflow in the vortex lattice. The curves are based on Eq. (22), the values of the numerical constants are from Refs. 38 and 44, the vortex core radius $\xi_c = \xi_0 = \hbar v_F/(k_B T_c)$ and the Wigner cell radius $r_v = 200\ \mu$m.

will have to be proportional to the cross-sectional area $\pi\xi_c^2$ of the core, it is necessary to gain information about the core structure, i.e., the order parameter distribution inside the core region. In contrast the flow contribution λ_f is only weakly sensitive to the core structure, since it depends logarithmically on r_v/ξ_c. Such a decomposition of the orientational effects from the vortices into extra- and intracore contributions is to some extent arbitrary. A more consistent treatment would call for a calculation of the overall parameter λ, which must appear in Eq. (20) instead of λ_f. Such a program has so far been realized only in the Ginzburg-Landau region[20,22] whereas the bulk of the experimental information has been obtained at temperatures far below T_c. Note that the estimate of λ_f in Eq. (22) is based on a hydrodynamic treatment (using additional information about the

orbital anisotropy of the magnetized ^{3}He-B) and the range of its validity is not limited to the vicinity of T_c.

Finally, summing up what has been said above, we come to the conclusion that the rotation-dependent orientational contribution to the density of the orbital anisotropy energy of the magnetized B-phase can be parametrized in the form

$$F_{an} = -aH^2[(\hat{\mathbf{n}} \cdot \hat{\mathbf{h}})^2 - \tfrac{2}{5}\lambda(P, T)(\hat{\mathbf{h}} \cdot \vec{\mathbf{R}}(\hat{\mathbf{n}}, \Theta_0) \cdot \hat{\boldsymbol{\Omega}})^2] \tag{23}$$

Here $\lambda(P, T)$ is used at this point as a phenomenological parameter which characterizes the global orienting effect on the $\hat{\mathbf{n}}$-field from the lattice of singular vortices. Although we do not have a theoretical description of the full behavior of λ at all pressures and temperatures, we have seen, nevertheless, that it includes the extra- and intracore contributions λ_f and λ_c. λ_f is nonmonotonic with respect to temperature and determines the overall shape of the $\lambda(T)$ curve. λ_c, on the other hand, is more directly related to the vortex core structure and as such may undergo discontinuous changes in abrupt rearrangements of the core. These structural transitions, in turn, must also be reflected via the parameter λ in Eq. (23) as sudden global textural changes. Furthermore, the two terms in Eq. (23) display competing orientational effects on the $\hat{\mathbf{n}}$-field. The first term (of dipole-dipole origin) favors parallel and antiparallel alignment of $\hat{\mathbf{n}}$ along the magnetic field, while the second term (from the averaged influence of the superflow circulating the vortex core and the magnetic anisotropy in the core) tends to counteract the establishing of the preferred spin-orbit configuration. The overall effect depends significantly on the relative orientations of $\mathbf{H}$ and $\boldsymbol{\Omega}$.

Equation (23) as such is not yet sufficient to explain the differences between the textures of the stationary and rotating states. It was first experimentally observed[21] that the NMR frequency shifts depend on the sense of rotation, i.e., whether the rotation is clockwise or anticlockwise at fixed magnetic field orientation. Consequently, a further free energy term linear in both $\mathbf{H}$ and $\boldsymbol{\Omega}$ had to be included into the analysis. This gyromagnetic contribution is written in the form

$$F_{gm} = \tfrac{4}{5}a\kappa(\mathbf{H} \cdot \vec{\mathbf{R}}(\hat{\mathbf{n}}, \Theta_0) \cdot \hat{\boldsymbol{\Omega}}) \tag{24}$$

and is explained to originate principally from a spontaneous intracore magnetization distribution. Thus the gyromagnetic parameter κ depends on the core structure, similar to λ_c. Present models for the vortex core structures at both low and high pressures in the Ginzburg–Landau region are in reasonable quantitative agreement with the experimental values for both λ_c and κ.[12,13,20,22]

Finally, we need to investigate how the free energy contributions of the rotating state expressed in Eqs. (23) and (24) influence the texture.

Consider the bulk liquid far from any container walls ($R \gg \xi_H$) in an axial field ($\mathbf{H} \| \mathbf{\Omega}$), then

$$F_{\text{an}} = aH^2\left[\left(1-\lambda \mp \frac{\kappa}{H}\right)\sin^2\beta + \frac{5}{8}\lambda \sin^4\beta\right] + \text{const} \tag{25}$$

where β is the angle between $\hat{\mathbf{n}}$ and $\mathbf{H}$. At equilibrium

$$\sin^2\beta = \begin{cases} 0, & \lambda \le 1 \mp \kappa/H \\ \frac{4}{5}\left(1 - 1/\lambda \pm \frac{\kappa}{H\lambda}\right), & \lambda \ge 1 \mp \kappa/H \end{cases} \tag{26}$$

where the upper sign applies to the case where $\mathbf{H}$ and $\mathbf{\Omega}$ are parallel while the lower sign refers to antiparallel alignment. Thus in the open geometry in the absence of walls there exists a threshold value $\lambda_{cr} = 1 \mp \kappa/H$ below which $\hat{\mathbf{n}} \| \mathbf{H}$ as in the absence of rotation. When the angular velocity builds up (recall that $\lambda \propto \Omega$) and the threshold λ_{cr} is reached, an orientational phase transition takes place to a state with $\beta \neq 0, \pi$. This is reflected in the appearance of a shift in the transverse NMR frequency relative to the Larmor frequency $\nu_0 = \gamma H/(2\pi)$ by an amount

$$\delta\omega_\perp = \frac{\omega_L^2}{2\omega_0}\sin^2\beta = \frac{2}{5}\frac{\omega_L^2}{\omega_0}(1 - 1/\lambda \pm \kappa/(\lambda H)) \tag{27}$$

The phase transition to the new state with $\beta \neq 0, \pi$ breaks the axial symmetry of the initial texture with $\hat{\mathbf{n}} \| \mathbf{H} \| \mathbf{\Omega}$, again a consequence from the broken spin-orbit symmetry.

In a real experiment, one always deals with a limited volume of ^{3}He-B such that the effect from the boundaries becomes important and the $\hat{\mathbf{n}}$-field is inhomogenous, as a rule. To account for the orienting effect of the walls, we have to include the gradient free energy which depends on certain spatial derivatives of the order parameter. For ^{3}He-B it is written in the form

$$\begin{aligned} F_{\text{text}} &= \frac{1}{2}\chi_B\left(\frac{c_\perp}{\gamma}\right)^2\left[\frac{1}{2}(\nabla_i R_{\mu i})^2 + \frac{1}{4}(\nabla_i R_{\mu j})^2\right] \\ &= \frac{5}{4}\chi_B\left(\frac{c_\perp}{\gamma}\right)^2\left\{(\nabla_i \hat{\mathbf{n}})^2 - \frac{1}{16}(\sqrt{3}\nabla \cdot \hat{\mathbf{n}} + \sqrt{5}\hat{\mathbf{n}} \cdot (\nabla \times \hat{\mathbf{n}}))^2\right\} \end{aligned} \tag{28}$$

where $c_\perp$ is the velocity of spin waves propagating in a direction transverse to $\hat{\mathbf{n}}$. In the literature the prefactor in the gradient energy is also written in the form $5\chi_B(c_\perp/\gamma)^2/4 = 16c/13$, where the bending stiffness coefficient $c = 65\chi_B(c_\perp/\gamma)^2/64$. To write down the total free energy density, it is convenient at this stage to introduce the magnetic healing length ξ_H as the

characteristic length scale with

$$\xi_H = \left(\frac{c}{a}\right)^{1/2} \frac{1}{H} = \left(\frac{65\chi_B}{64a}\right)^{1/2} \frac{c_\perp}{\gamma H} \tag{29}$$

We then find in natural energy units aH^2 for the axial field orientation

$$f_{\text{an}} = (1 - \lambda \mp \kappa/H) \sin^2 \beta + \tfrac{5}{8}\lambda \sin^4 \beta \tag{30a}$$

$$f_{\text{text}} = \frac{16}{13} \xi_H^2 [(\nabla_i \hat{\mathbf{n}})^2 - \tfrac{1}{16}(\sqrt{3}(\boldsymbol{\nabla} \cdot \hat{\mathbf{n}}) + \sqrt{5}\hat{\mathbf{n}} \cdot (\boldsymbol{\nabla} \times \hat{\mathbf{n}}))^2] \tag{30b}$$

where it proves useful to introduce the notation $\xi'_H = (16/13)^{1/2}\xi_H$. The equilibrium distribution of the $\hat{\mathbf{n}}$-field is found by minimizing the volume integral

$$\int (f_{\text{an}} + f_{\text{text}})\, d^2r$$

with the appropriate boundary conditions as imposed by the container walls. The perfect axially symmetric experimental arrangement leads to the flare-out texture, shown in Fig. 1, which we shall next briefly describe.

2.2. Flare-Out Texture

The flare-out texture represents the minimum energy $\hat{\mathbf{n}}$-field configuration in a cylindrical container with the magnetic field oriented along the symmetry axis. In the stationary state, it results from the competition of three different textural free energy terms: the magnetic anisotropy energy δF_{DH} given by Eq. (8), the gradient energy F_{text} in Eq. (28), and the surface energy F_{surf} (cf. Ref. 15). F_{surf} fixes the orientation of $\hat{\mathbf{n}}$ at the wall such that the polar angle $\beta = \arccos(1/\sqrt{5}) \simeq 63.4°$ and the azimuthal angle $\alpha = 60°$ (cf. Fig. 2). δF_{DH} attempts to deflect $\hat{\mathbf{n}}$ towards the external field direction while the ratio $\delta F_{DH}/F_{\text{text}}$ specifies the rate at which the wall orientation may change towards the bulk orientation on moving away from the wall. The gradual recovery of the bulk orientation is governed by the magnetic healing length ξ_H but is strictly speaking fully established only on the cylinder axis. In the rotating state, the bulk liquid anisotropy energies have to be augmented by the vortex free energy F_v given by the second term in Eq. (23), and by the gyromagnetic contribution F_{gm} in Eq. (24).

The structure of the flare-out texture was first numerically investigated by Maki and Nakahara.[23] They used an approximate approach according to which the aximuthal angle was fixed at $\alpha = 60° = \text{const.}$ independent of the radius r, while Hakonen and Volovik[24] used the infinite R approximation in which the cylindrical surface is replaced by a plane boundary. The first rigorous numerical solution was obtained by Jacobsen and Smith.[25] We

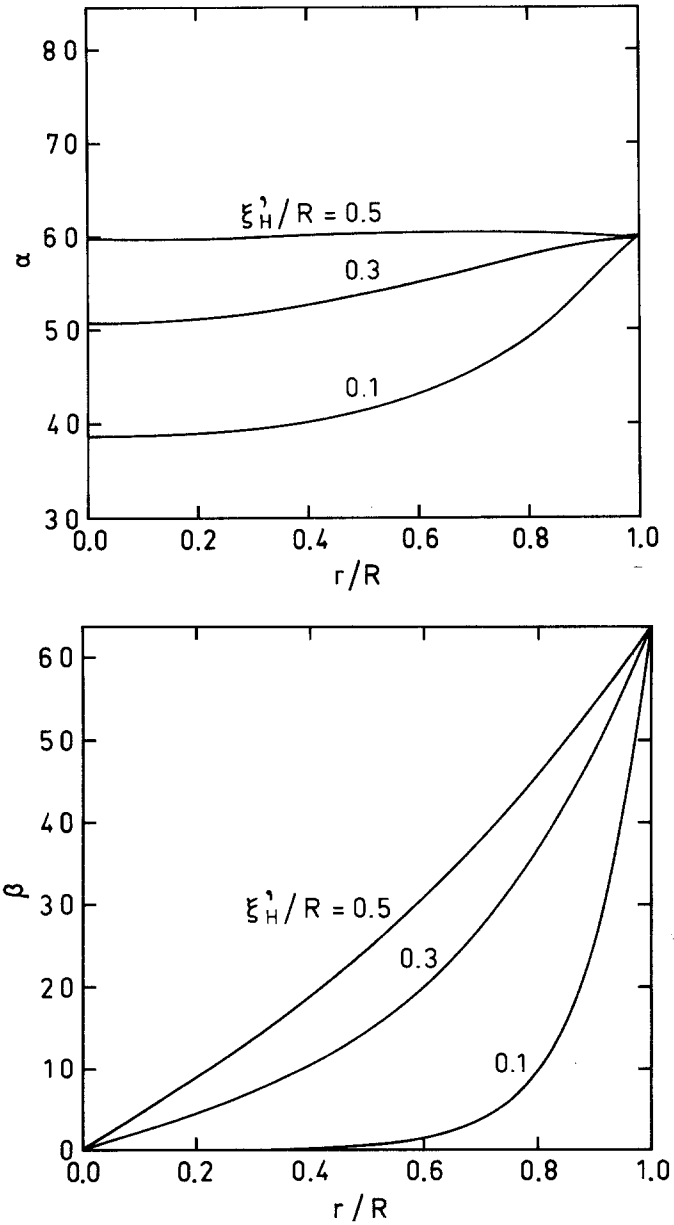

Fig. 3. Orientation of $\hat{\mathbf{n}}$ in the flare-out texture as a function of the normalized radial distance r/R for three different values of the magnetic healing length ξ'_H: (bottom) azimuthal angle α and (top) polar angle β. The boundary conditions at the cylinder wall are: $\alpha = 60°$ and $\beta = 63.4°$.

have repeated these calculations and have extended the range of values for the various parameters in order to permit a more detailed comparison between calculation and experiment. The results are schematicaly illustrated in Fig. 2, while Figs. 3a and 3b display the variations of $\alpha(r)$ and $\beta(r)$ with three different values of ξ'_H. The $\alpha(r)$ curves are relatively flat, particularly for large ξ'_H. The $\beta(r)$ curves incorporate two limiting regions: 1) at small r, $\beta(r)$ displays a linear dependence with $\beta = \beta_1 r$, where β_1 is a constant slope, while 2) on approaching the wall at $r = R$, the dependence becomes exponential and is roughly given by $\beta(r) \propto \text{arc cos}(1/\sqrt{5}) \exp[-(R-r)/\xi'_H]$. With increasing rotation velocity Ω, the polar angle β opens up at any given radius r until it finally approaches the bulk liquid value (given by Eq. (26) for $\lambda > \lambda_{cr}$ and shown in Fig. 17a) as a plateau in the $\beta(r)$ curves, particularly when λ is large and ξ'_H small.

The linear region of $\beta(r)$ in the central part of the texture plays an important role in the NMR properties: the slowly varying textural inhomogeneity traps standing spin-wave excitation modes which leave clearly distinguishable resonance absorption peaks in the transverse cw NMR spectrum. The spacing between these absorption peaks follows accurately the eigenvalue spectrum of a harmonic oscillator and allows a direct determination of the harmonic potential, i.e., the slope β_1. The first NMR measurements of B-phase textures were performed in cylindrical geometry,[26] and later in parallel plate geometries[27,28] in order to simplify comparison between experiment and theory. Subsequently, also the spin-wave absorption modes were discovered,[17] when the static field homogenity was sufficient and a suitable spacing was selected between planes in a stack of the parallel plates. The spin-wave resonances were again prominently featured in the first texture measurements in the rotating state[2,4] in the cylindrical geometry and have since then become one of the basic tools for investigating ^{3}He-B in rotation.

In the following we consider the cw NMR spectrum from the flare-out texture to illustrate the procedure for extracting detailed data about the texture. There are two features in the NMR spectrum which are of importance here: 1) the general shape of the resonance absorption envelope, as generated by the frequency shifts obeying local oscillator behavior, and 2) the spin-wave absorption peaks, generated by collective, nonlocal oscillator behavior.

2.3. NMR Spectrum

In transverse cw NMR, the resonance frequency ν is shifted from the Larmor value $\nu_0 = \gamma H/(2\pi)$ according to the formula[16,17]

$$\nu^2 = \tfrac{1}{2}(\nu_0^2 + \nu_L^2) + [\tfrac{1}{4}(\nu_0^2 + \nu_L^2)^2 - \nu_0^2 \nu_L^2 \cos^2 \beta]^{1/2} \tag{31}$$

where $2\pi\nu_L = \omega_L(P, T)$. In the high-field limit $\nu_0 \gg \nu_L$, a fair approximation to the measured transverse resonance frequency ν is obtained from

$$\nu = \nu_0 + \frac{\nu_L^2}{2\nu_0} \sin^2\beta \left[1 + \left(\frac{\nu_L}{\nu_0}\right)^2 \cos^2\beta \right] \tag{32}$$

where even the factor in the brackets may usually be set equal to 1. The measured transverse frequency shift $\nu - \nu_0$ is thus determined by the polar angle β in a straightforward manner. Adopting this local oscillator picture, according to which every part of the sample is supposed to resonate at a frequency determined by the local value of β, the averaged envelope of the NMR spectrum is directly generated by the $\hat{\mathbf{n}}$-field texture such that the absorbed resonance power per frequency interval is proportional to

$$P(\nu) \propto \frac{2}{R^2} \int_0^R r\, dr\, \delta(\nu - \nu(r)) \tag{33}$$

Here $\nu(r) \sim \nu_0 + (\nu_L^2/2\nu_0) \sin^2\beta(r)$ and thus $P(\nu) \propto (2/R^2)[\partial \sin^2\beta/\partial r^2]^{-1}$.

Some examples of local oscillator absorption spectra are shown in Fig. 4. These have been calculated for the three different flare-out textures shown in Fig. 3, neglecting all line broadening from field inhomogeneity and

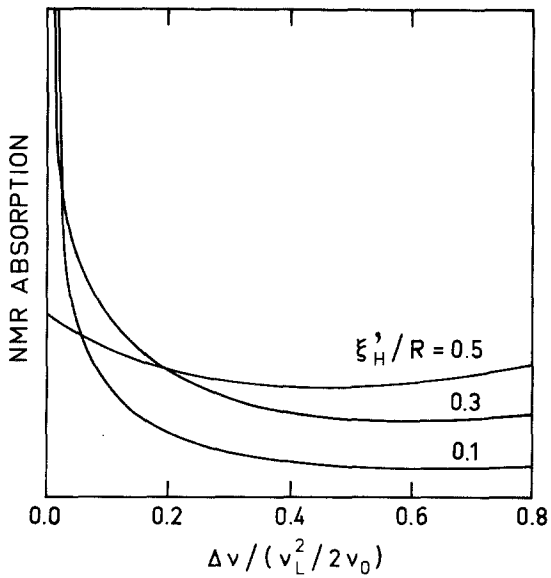

Fig. 4. Calculated local oscillator resonance absorption as a function of the scaled frequency shift $(\nu - \nu_0)2\nu_0/\nu_L^2$ for three different values of the magnetic healing length ξ'_H.

relaxation. At small values of ξ_H, the NMR absorption $P(\nu)$ is characterized by a sharp maximum, which borders to the low-frequency cutoff at ν_0 and originates from the central region of the texture. This absorption peak is followed by a long tail towards the high-frequency edge corresponding to the wall orientation with the maximum value of $\beta = 63.4°$. With increasing ξ_H more and more of the resonance absorption is shifted to higher frequencies as the slope of $\beta(r)$ grows in the central part of the texture (cf. Fig. 3). On comparing the calculated absorption spectra with measured signal envelopes, we observe a fair resemblance between the $\xi'_H = 0.5$ R curve in Fig. 4 and the stationary state signal in the top part of Fig. 5. This latter signal envelope has been measured at a low pressure of 10.2 bar and a low temperature of $T = 0.53\ T_c$, where ξ'_H becomes as large as $0.5\ R \sim 1$ mm (cf. Fig. 13). The signal in the lower section of Fig. 5 has been measured in the rotating state and illustrates how the absorption shifts to higher frequencies with increasing λ when the region with small β values in the centre of the cylindrical container shrinks (cf. Fig. 17).

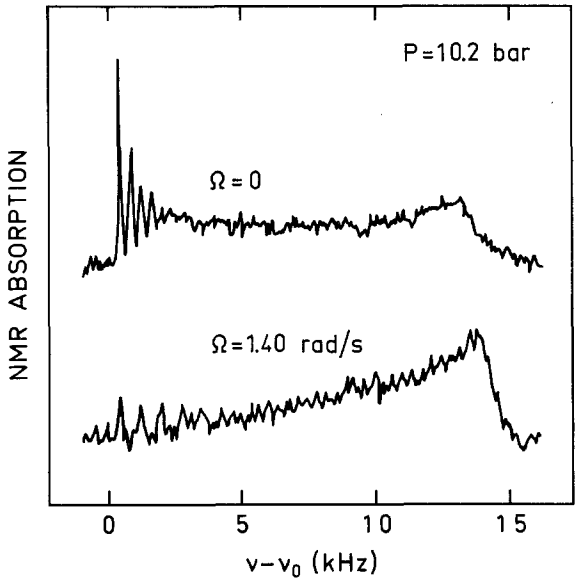

Fig. 5. Measured NMR absorption signal envelopes from a flare-out texture: $H = 28.4$ mT (i.e., $\nu_0 = 922.5$ kHz), $P = 10.2$ bar, and $T = 0.53\ T_c$. The horizontal axis is the frequency shift measured in kHz from the Larmor frequency ν_0. The sharp peaks close to the Larmor edge are the spin-wave resonance absorption modes. The high-frequency edge is fixed by the wall orientation requiring $\beta = \arccos(1/\sqrt{5})$.

While the general shape of the NMR signal envelope rather faithfully obeys the simple local oscillator picture, the sharp spin-wave absorption modes close to the Larmor edge in Fig. 5 can only be explained on the basis of a more accurate treatment of Leggett's general equations of spin dynamics.[15,17] In particular we need to allow for global, coherent spin precession which, in the high-field limit, can be reduced to a single equation describing the motion of the transverse spin operator $S_+ = S_x + iS_y$:

$$[-\tfrac{48}{65}\xi_D^2\nabla^2 + \sin^2\beta(r)]S_+ = ES_+ \tag{34}$$

In this Schrödinger-like equation, the length scale is set by the dipolar length ξ_D, which is defined as

$$\xi_D = \left(\frac{65}{32}\right)^{1/2}\frac{c_\perp}{\omega_L} = \left(\frac{2c\gamma^2}{\chi_B\omega_L^2}\right)^{1/2} = \left(\frac{13}{24}\right)^{1/2}\frac{\hbar}{2mv_D} \tag{35}$$

The units for the eigenvalues E are given in terms of a relative frequency shift

$$E = \frac{2\nu_0}{\nu_L^2}(\nu - \nu_0) \tag{36}$$

The equation applies for a situation where the inclination of $\hat{\mathbf{n}}$ from the external field direction remains small, like in the region close to the cylindrical symmetry axis. In this part of the texture, $\beta(r)$ is linear with a small slope, such that $\sin\beta(r) \simeq \beta_1 r$, and Eq. (34) reduces to that of a harmonic oscillator. Thus the eigenvalues are given by the equally spaced harmonic spectrum

$$E_n = 2(n+1)(\tfrac{48}{65})^{1/2}\xi_D\beta_1, \qquad n = 0, 1, 2, \ldots \tag{37}$$

However, with homogeneous static polarizing and rf excitation fields only modes with even parity are excited and $n = 0, 2, 4, \ldots$. These levels are $n+1$ fold degenerate; however, again only the modes $e^{im\phi}$ with $m = 0$ are excited. The relative intensities of the modes are determined from

$$I_n \propto \frac{1}{R^2}\left|\int S_+^{(n)} r\,dr\right|^2 \Big/ \int |S_+^{(n)}|^2\, r\,dr$$

A particular property of the two-dimensional oscillator is that $I_n/I_0 = 1$. The width of the resonances is proportional to $n+1$ and thus only the lowest modes are discernible.[23]

The harmonic approximation is expected to be sufficient as long as the radius of localization for the spin-wave excitation modes remains small, *i.e.*, $(\xi_D/\beta_1)^{1/2} \ll \xi_H'$. In practice the experimentally observable spin-wave absorption peaks turn out to follow rather closely the harmonic spectrum. More generally, however, Eq. (34) should be solved with the appropriate potential well $\sin^2\beta(r)$ which has been plotted in Fig. 6 for the flare-out

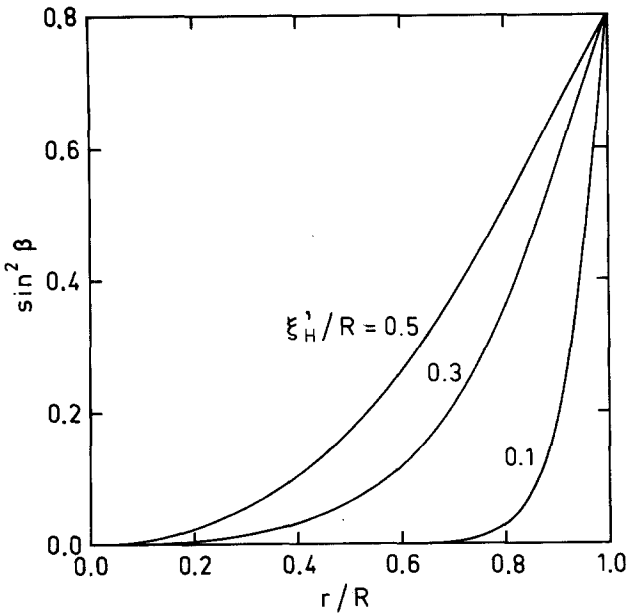

Fig. 6. Calculated spin-wave potentials of the flare-out texture for the spin-wave Eq. (34).

textures of Fig. 3. Figure 7 presents the energy eigenvalues E_n of the ten lowest eigenmodes as a function of ξ'_H/R with $\xi_D = 10\,\mu$m. The lowest three modes obey the harmonic oscillator-like spectrum accurately in the region $\xi'_H/R \gtrsim 0.3$.

In principle the width of the spin-wave absorption lines can be used to determine the spin diffusion coefficient D of the bulk liquid, unaffected by the presence of the walls, because the modes are located around the cell axis. Simple perturbation analysis, neglecting all off-diagonal elements, yields for the linewidth $2(n+1)\beta_1 D/(2\pi\xi_D\sqrt{f})$ in units of frequency. Experimentally, D is found from the NMR spectrum by finding the ratio between the position of the spin-wave line (cf. Eq. (37)) and its width, since this ratio is simply given by $\pi\xi_D^2 f\nu_L^2/(\nu_0 D)$ with $f = 48/65$, and only requires knowledge about the dipole length. Owing to the increasing linewidth of the modes, the amplitude of the spin-wave resonances falls off as $1/(n+1)$. Figure 8 displays two examples of spin-wave spectra obtained by adding equally spaced Lorentzian lines with linewidths increasing as $n+1$ ($n = 0, 2, 4, \ldots$). Such spin-wave spectra can be constructed to match the measured spin-wave resonance absorption shown in Fig. 5.

The effect of rotation is to increase the frequency spacing of the modes while spin diffusion remains unchanged (cf. Sec. 4.2.).

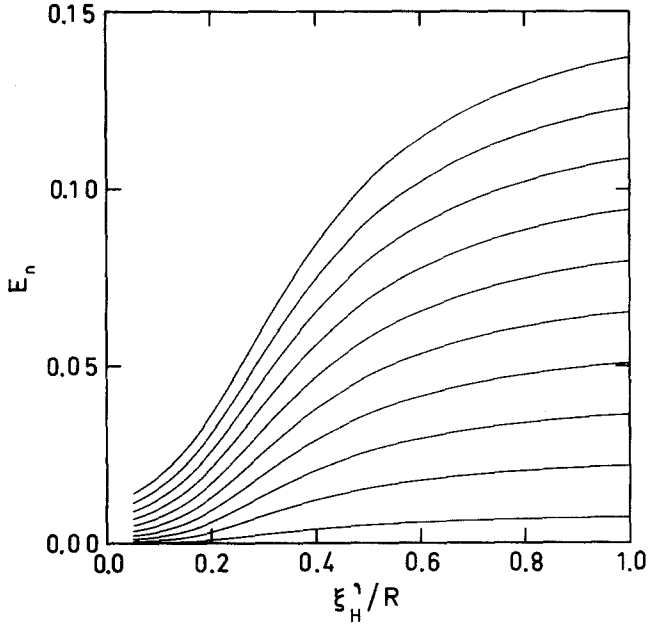

Fig. 7. Calculated spin-wave spectrum, given in the dimensionless units of Eq. (37) and plotted as a function of the normalized magnetic healing length ξ'_H/R. The dipole length $\xi_D = 10\ \mu$m.

3. RESULTS IN THE STATIONARY STATE

3.1. Experimental Details

The experimental apparatus and techniques have been described in Refs. 4, 29, and 30. The liquid ^{3}He sample is cooled to superfluid temperatures in a rotating nuclear demagnetization cryostat.[29] The sample is contained in a long cylindrical epoxy tower with a radius $R = 2.5$ mm. At its bottom end, the tower connects to a copper cell with a sintered silver heat exchanger for thermal contact to the copper refrigerant. A saddle-shaped coil, consisting of two rectangular halves, is wound around the upper end of the tower and is used for the superfluid ^{3}He NMR. An additional solenoidal NMR coil, with its axis oriented transverse to the cryostat axis, is located directly above the ^{3}He tower and is filled with a liquid ^{3}He sample at the same liquid pressure but higher temperature. This NMR coil is thermally anchored to the mixing chamber of the precooling ^{3}He/^{4}He-dilution refrigerator and provides a simultaneous reference signal at the Larmor frequency. The axial polarizing field is generated with an

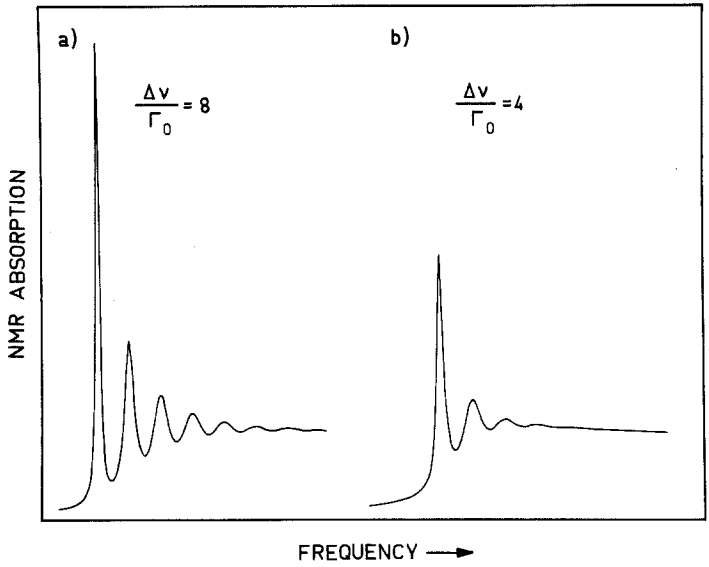

Fig. 8. Simulated spin-wave resonance spectra formed by summing 40 Lorentzian lines with equal integrated intensities and a constant frequency spacing $\Delta\nu$. The half-width Γ_n (full width at half of maximum amplitude $= 2\Gamma_n$) of a line increases with the order number as $n+1$.

end-compensated superconducting solenoid located outside the vacuum jacket in the liquid He bath. Its field inhomogeneity is $\Delta H/H \sim 4\times 10^{-5}$ over the NMR sample.

The transverse continuous wave NMR signals from both the superfluid ^{3}He-B sample and from the Fermi liquid reference are recorded in parallel using two independent spectrometers and a linear, triangular field sweep.[30] Thus the Fermi-liquid reference indicates the relative location of the Larmor frequency during each field sweep and diminishes drift problems associated with the polarizing field and the sweep. In addition, the scaling factor of the frequency axis, the longitudinal resonance frequency $\nu_L(P, T)$, is directly determined from each individual NMR spectrum of the flare-out texture, which further reduces errors, in particular due to variations in temperature scales between different experiments. In part, this procedure was also a necessity since, to our knowledge, there exists no published data on $\nu_L(P, T)$ at low pressures which would satisfy our needs. The temperature is determined from the integrated intensity of the nuclear free precession signal of platinum powder immersed in the ^{3}He-B liquid, measured by means of pulsed NMR at a fixed field value during every second field sweep. Only the linearity of the inverse nuclear susceptibility with temperature is of importance in the ^{195}Pt NMR measurement since all temperatures in this

work are specified on the relative T/T_c scale. The Pt NMR signal corresponding to T_c is determined separately for each cool-down and warm-up by following the evolution of the ^{3}He NMR signal during the thermal sweep through T_c.

The present axial field measurements have been performed at 28.4 and 56.9 mT. The rotation velocities extend up to 2.0 rad/sec. The measurements cover a liquid ^{3}He pressure range of 0.5–29 bar. In all cases the object has been to investigate an equilibrium distribution of vortices. This is accomplished by rotating the cryostat intermittently, i.e., it is accelerated from rest to the desired rotation velocity at each temperature where measurements are performed using a carefully monitored start-stop routine. Spin-wave resonance absorption has been studied at 28 mT mainly at the higher pressures of 10–29 bar while line shape analysis has been the principal tool at the lower pressures of 0.5–10 bar, also at 28 mT. As a further cross check we have also employed the line shape analysis technique at 0.5 and 25 bar in the higher magnetic field of 57 mT. From the stationary state measurements, three central parameters have been determined, namely the longitudinal resonance frequency $\nu_L(P, T)$, the magnetic healing length $\xi_H(P, T)$ and the dipolar coherence length $\xi_D(P, T)$. In addition, some representative values of more qualitative nature will be given for the effective spin-diffusion coefficient $D(P, T)$. These parameters control the flare-out texture and are essential for the analysis of the rotating state textures in order to extract representative values for the λ and κ parameters.

3.2. Longitudinal Resonance Frequency

An accurate determination of the longitudinal resonance frequency $\nu_L(P, T)$ from the NMR signature of a flare-out texture is a delicate question. In Fig. 9 three different NMR signal envelopes are shown. The first one, (a), corresponds to a situation where the flare-out texture is defective and includes a soliton wall.[31] The stationary soliton produces a square root singularity in the absorption spectrum at the frequency corresponding to $\beta = \pm\pi/2$, *i.e.*, when the condition $\hat{\mathbf{n}} \cdot \mathbf{H} = 0$ is fulfilled. The location of the soliton peak on the frequency axis has been used to identify $\nu_L(P, T)$ according to Eq. (32). This value for ν_L locates the frequency corresponding to $\beta = \pm 63.4°$ at the extrapolated endpoint of the envelope of signal (b) in Fig. 9. This line shape, which represents a clean flare-out texture, is obtained from the soliton-contaminated signal after a rapid acceleration at 0.1 rad/sec^2 or more. In passing, it is useful to note that acceleration or deceleration of rotation is a very effective means of annealing defects from textures in both the A- and B-phases. Subsequently after loosing the soliton anomaly, the identification indicated in Fig. 9(b) was employed for extracting ν_L from the flare-out signal envelopes.

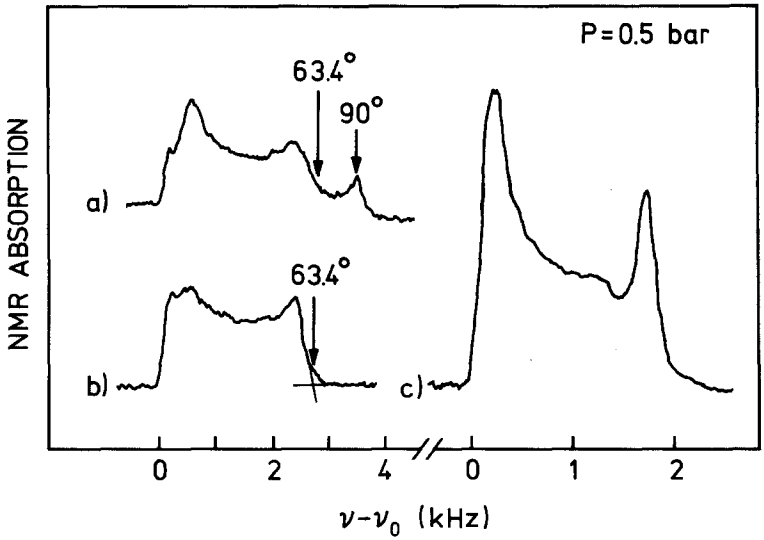

Fig. 9. NMR absorption signals measured at 0.5 bar and 28.4 mT: a, Line shape at $0.77T_c$ for a sample which has not yet been rotated; the absorption peak at $\beta = 90°$ is produced by stationary soliton-like textural defects; b, after acceleration at a rate of 0.1 rad/sec^2, the clean flare-out signal emerges and is shown here for the stationary state; c, at high temperatures ($T = 0.85T_c$) the signal is distorted by a peak at the high-frequency end which is believed to be an artifact of the measurement.

Closer to T_c the high-frequency tail developed into a second maximum as shown in Fig. 9(c). This anomalous absorption peak is believed to be caused mainly by the inhomogeneity of the rf excitation field H_1, generated by the saddle-shaped coil on the ^{3}He tower. The value of H_1 increases monotonically towards the wall but the rate of increase depends strongly on the azimuthal angle. It is possible that part of the sample is driven close to saturation or in a nonlinear fashion near some wall locations.[32] At any rate, even here the extrapolation procedure of Fig. 9(b) appears to give reasonable values for ν_L which were first identified as the longitudinal resonance frequency in direct measurements of the longitudinal resonance at the melting pressure in Ref. 33.

In Fig. 10 a summary is shown of the $\nu_L(p, T)$ determinations from the present measurements. At 5.0, 10.2, and 15.5 bar ν_L has been identified exclusively from the soliton peak which yields the most reliable results. At 0.5 and 25.0 bar, both the soliton peak and the high-frequency edge of the flare-out signal envelope have been used for the identification and consequently these results should be viewed in the light of larger uncertainty limits. Nevertheless, the 25.0 bar data can be compared to earlier NMR measurements in Ref. 16; the agreement appears to be satisfactory: at most

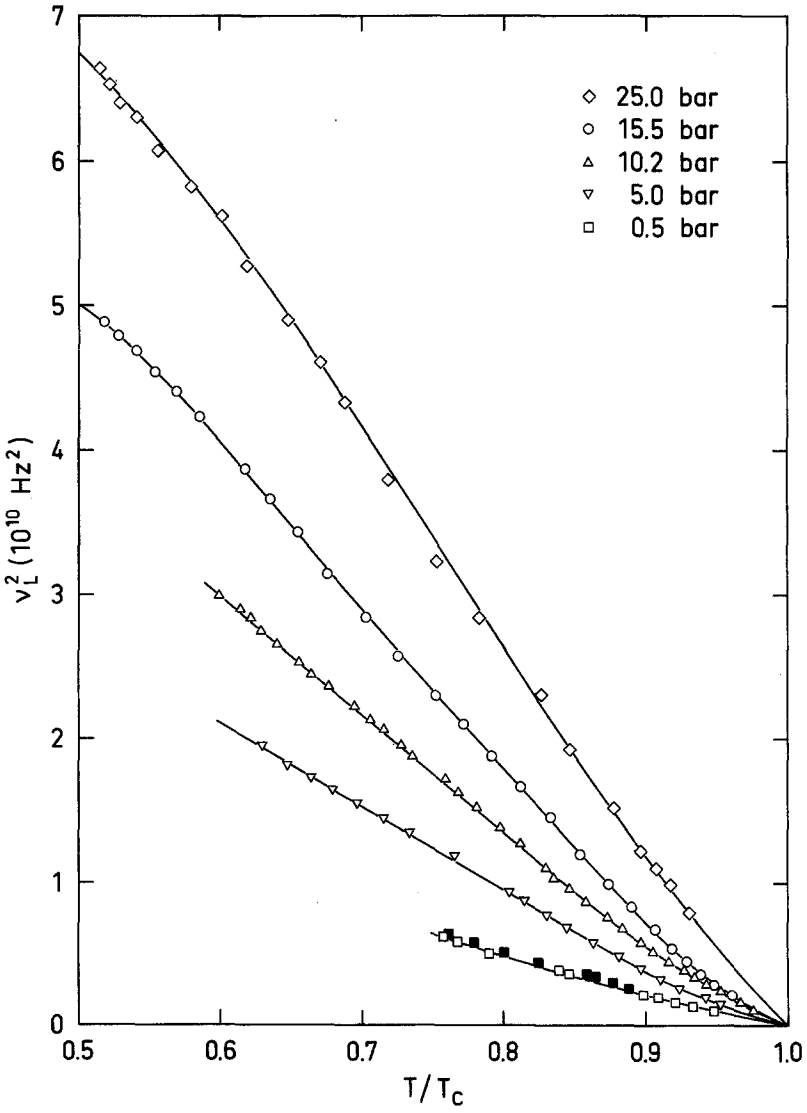

Fig. 10. Isobars of the square of the B-phase longitudinal resonance frequency $\nu_L(P, T)$ vs. temperature. At 0.5 bar results have been included from both the stationary (open squares) and rotating states (filled squares).

a 4% shift to larger ω_L^2 values could be present in the new data. Such a difference, however, is of the same magnitude as the uncertainty in the data.

Close to T_c and for $P \leq 15.5$ bar the data in Fig. 10 can be approximately expressed with the formula

$$\nu_L^2 = \frac{(0.26P + 1.7)(1 - T/T_c)}{1 - 1.7(1 - T/T_c)} 10^{10} \text{ Hz}^2 \tag{38}$$

The smoothed data do not deviate by more than ±8% from this expression in the range from 0.8 T_c to T_c. Unfortunately, the results close to T_c are extremely sensitive as to which Pt NMR reading is selected to correspond to T_c. This correspondence can only be determined up to a point since 1) it is only at T_c that any changes in the Fermi-liquid signal start to develop, and 2) signal recovery with fine absorption details requires a slow field sweep matched to a correspondingly slow temperature sweep through T_c such that the linearity of the latter sweep becomes a difficulty. A 0.5% error in the Pt NMR reading of T_c would change the slope of ν_L^2 as a function of $1 - T/T_c$ by 10%. We believe that our T_c determinations are correct to within ±1%.

In Fig. 11 isotherms of $\nu_L(P, T)$ are shown. The smooth and monotonically increasing curves are parabolic least-squares fits to the data. These curves have been used to provide the $\nu_L(P, T)$ values needed in the subsequent data analysis. At 29.3 bar the data from Ref. 16 have been used. In Fig. 11 we have also included the results from Refs. 16 at 18.7, 21.1, and 25.4 bar. These measurements drop below the present ones towards decreasing pressure: the maximum difference can be found at 18.7 bar which is the lowest pressure of the earlier measurements. There the deviation is 10% at $0.8T_c$ and 7% at $0.6T_c$.

Leggett[34] gives a consistency check for the ratio of the longitudinal resonance frequencies in the A- and B-phases:

$$[\nu_L^{(B)}/\nu_L^{(A)}]^2 = \frac{5}{2} \frac{\chi_A}{\chi_B} \left(\frac{\Delta_B}{\Delta_A}\right)^2 \tag{39}$$

Close to the polycritical point at 21.2 bar, this ratio is simply 5/2. On comparing our $\nu_L^{(B)}(P, T)$ data to the A-phase longitudinal frequencies $\nu_L^{(A)}(P, T)$ from Ref. 16, the ratio in (39) becomes 2.80, while the A-phase ringing frequencies of Webb *et al.*[35] yield a ratio of 2.16. Thus we conclude that within about ±10% the consistency requirement appears to be satisfied. Unfortunately, we have not measured the A-phase frequencies $\nu_L^{(A)}(P, T)$ at the lower pressures in the present experimental set-up (however, for 29.3 bar data are given in Ref. 30).

Close to T_c the slope of ν_L^2 vs $1 - T/T_c$ can be used to study strong coupling corrections to the energy gap. This has previously been done in

TABLE I

Measured values of the B-phase longitudinal resonance frequency $\nu_L(P, T)$: listed as ν_L^2 vs. temperature at various pressures[a]

$P = 0.5$ bar		$P = 5.0$ bar		$P = 10.2$ bar		$P = 15.5$ bar		$P = 25.0$ bar	
T/T_c	ν_L^2 (10^9 Hz^2)	T/T_c	ν_L^2 (10^{10} Hz^2)	T/T_c	ν_L^2 (10^{10} Hz^2)	T/T_c	ν_L^2 (10^{10} Hz^2)	T/T_c	ν_L^2 (10^{10} Hz^2)
0.762	6.14	0.627	1.959	0.598	2.982	0.475	5.167	0.502	6.695
0.762	6.30[b]	0.637	1.870	0.613	2.895	0.480	5.144	0.514	6.635
0.769	5.88	0.656	1.766	0.621	2.837	0.483	5.075	0.521	6.522
0.777	5.84[b]	0.679	1.636	0.625	2.760	0.487	5.104	0.528	6.398
0.791	5.09	0.697	1.544	0.635	2.698	0.495	5.043	0.540	6.300
0.795	5.14[b]	0.715	1.438	0.645	2.613	0.506	4.967	0.555	6.070
0.815	4.82[b]	0.734	1.351	0.655	2.528	0.517	4.890	0.578	5.820
0.837	3.86	0.743	1.299	0.663	2.445	0.527	4.797	0.600	5.615
0.847	3.65	0.765	1.176	0.676	2.358	0.540	4.691	0.618	5.275
0.867	3.35[b]	0.810	0.896	0.687	2.263	0.553	4.541	0.647	4.895
0.885	2.77[b]	0.835	0.741	0.697	2.210	0.568	4.407	0.670	4.604
0.902	2.14	0.848	0.661	0.703	2.127	0.584	4.227	0.687	4.326
0.919	1.69	0.864	0.579	0.712	2.083	0.602	3.994	0.718	3.791
0.941	1.18	0.881	0.494	0.720	2.003	0.617	3.872	0.752	3.223
		0.893	0.420	0.728	1.947	0.634	3.659	0.782	2.833
		0.905	0.350	0.734	1.877	0.654	3.426	0.826	2.305
		0.916	0.300	0.759	1.708	0.675	3.143	0.846	1.925

0.927	0.249	0.768	1.618	0.704	2.835	0.877	1.513
0.940	0.200	0.780	1.515	0.725	2.572	0.896	1.220
0.950	0.151	0.792	1.420	0.752	2.300	0.907	1.095
		0.800	1.348	0.771	2.101	0.917	0.985
		0.811	1.274	0.791	1.882	0.930	0.790
		0.831	1.085	0.812	1.661		
		0.838	1.008	0.833	1.452		
		0.848	0.940	0.855	1.191		
		0.855	0.883	0.874	0.988		
		0.864	0.818	0.890	0.828		
		0.875	0.735	0.907	0.673		
		0.885	0.665	0.919	0.533		
		0.895	0.588	0.929	0.449		
		0.905	0.513	0.939	0.362		
		0.917	0.440	0.948	0.283		
		0.931	0.363	0.961	0.213		
		0.941	0.300				
		0.953	0.243				
		0.964	0.173				
		0.974	0.107				

[a] The slopes $\partial \nu_L^2 / \partial (1 - T/T_c)$ at T_c are: $P = 0.5$ bar, $1.9 \cdot 10^{10}$ Hz^2; $P = 5.0$ bar, $2.9 \cdot 10^{10}$ Hz^2; $P = 10.2$ bar, $4.7 \cdot 10^{10}$ Hz^2; $P = 15.5$ bar, $5.6 \cdot 10^{10}$ Hz^2; and $P = 25.0$ bar, $10.5 \cdot 10^{10}$ Hz^2. The corresponding values, when smoothed with respect to pressure, are: 1.7, 3.0, 4.5, 6.25, and $9.8 \cdot 10^{10}$ Hz^2.
[b] Rotating.

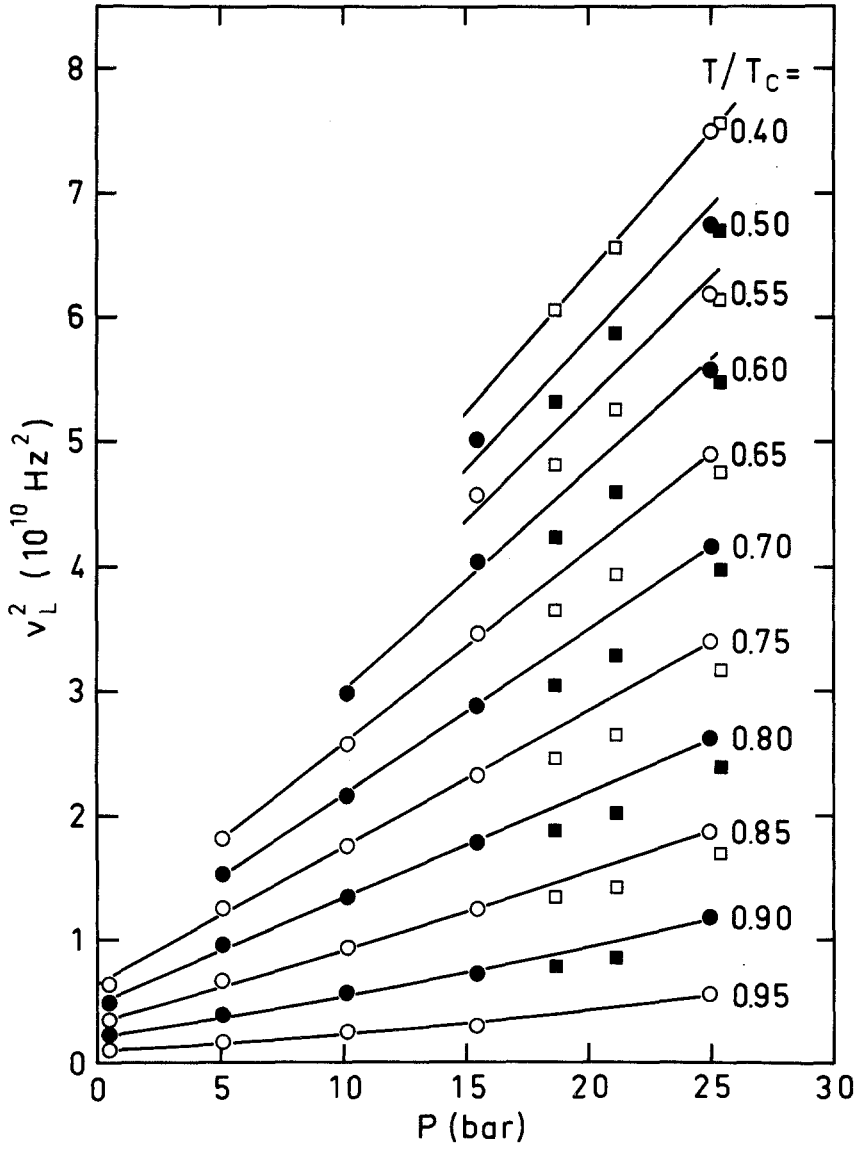

Fig. 11. Isotherms of the square of $\nu_L(P, T)$ plotted as a function of pressure. The data points have been read from the smooth curves drawn through the measurements in Fig. 10. Circles correspond to present data while squares represent earlier measurements from Ref. 16. The curves are parabolic fits to present results.

the A-phase where the strong coupling effects, which gain in importance towards high pressures, can be more readily extrapolated to T_c (see, e.g., Ref. 16). The longitudinal resonance frequency can be expressed in the form

$$\nu_L^2 \propto K(P)\left(\frac{\Delta(P,T)}{k_B T_c}\right)^2 \frac{\chi_N}{\chi_B} \tag{40}$$

Here $K(P)$ is a pressure dependent factor which involves the Landau parameter F_0^a and the density of states $N(0)$ at the Fermi surface, among others.[34] At low temperatures χ_N/χ_B is almost independent of pressure and thus the pressure dependence of $K(P)$ can be obtained from the low temperature limiting values of $\nu_L(P, T=0)$ and the calculated pressure dependence of $\Delta(P, T=0)/(k_B T_c)$.[36] Close to T_c, $\Delta^2 \propto k_B^2 T_c^2(1-T/T_c)\Delta C/C_>$ where $\Delta C/C_>$ is the B-phase specific heat discontinuity at T_c. Extrapolating to T_c one obtains $\Delta C/C_> \propto \nu_L^2/[(1-T/T_c)K]$. At vapor pressure, the specific heat jump is known to be close to the BCS weak coupling value of 1.42, while with increasing pressure the strong coupling effects result in an approximately linear increase of $\Delta C/C_>$ with liquid density. We find that $\Delta C/C_>$ increases by $(23 \pm 10)\%$ from 0 to 25.0 bar. In this comparison the values measured at $0.6T_c$ had to be used for $\nu_L(p, T=0)$. Nevertheless, the result is consistent with three different specific heat measurements which all give an increase of 29% over the same pressure range.[37-39]

In conclusion we observe that the present measurements of the B-phase longitudinal resonance frequency $\nu_L(P, T)$ appear to be both consistent and as a whole in agreement with other measurements. Measured values of $\nu_L(P, T)$ have been listed in Table I.

3.3. Magnetic Healing Length

Once the longitudinal resonance frequency ν_L has been determined the local oscillator approach can further be used to extract the magnetic healing length ξ_H from an analysis of the line shape. A direct comparison of the measured and calculated line shapes is complicated by experimental artifacts such as inhomogeneities in the rf excitation or the static polarizing fields (cf. Fig. 9c). In view of these difficulties we have chosen a relatively coarse procedure for determining ξ_H such that the results would be as insensitive as possible to minor line shape aberrations. In the following we use the notations ξ_H and $\xi'_H = (16/13)^{1/2}\xi_H$ in parallel.

As indicated in the inset of Fig. 12, the resonance absorption is integrated separately over two sections A and B of the $\sin^2\beta = (\nu-\nu_0)2\nu_0/\nu_L^2$ axis: the first interval is $0 < \sin^2\beta < X$ and the second $X < \sin^2\beta < 0.8$, where, as a consistency test, the division X has been given

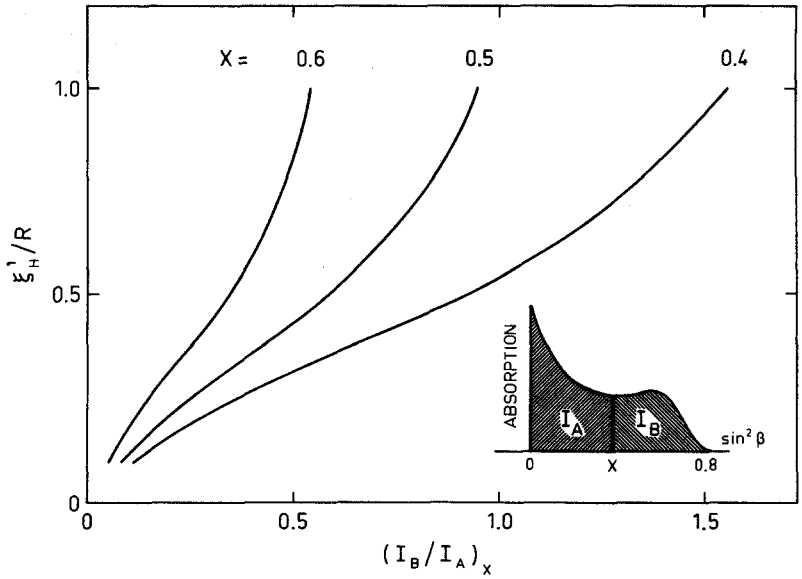

Fig. 12. Outline of the procedure for determining the magnetic healing length ξ_H' from a comparison of the measured NMR absorption signal with the calculated local oscillator spectrum. The NMR absorption is integrated separately over two sections of the scaled frequency axis $(\nu-\nu_0)2\nu_0/\nu_L^2$, as shown in the inset. In this plot the ratio of the calculated integrated intensities $(I_B/I_A)_X$ is shown as a function of the magnetic healing length ξ_H' for three different values of the division point X.

different values such as 0.4, 0.5, and 0.6. The ratio $(I_B/I_A)_X$ determined from a measured NMR signal is then compared with corresponding ratios obtained for calculated local oscillator absorption spectra which have been computed with a known value of ξ_H. The latter calculated ratios are read from graphs shown in Fig. 12 where $(I_B/I_A)_X$ has been plotted as a function of ξ_H for three different choices of the division X.

In Fig. 13 the results for ξ_H are shown at three different pressures 0.5, 5.0, and 10.2 bar in a magnetic field of 28.4 mT. Obviously, the choice of the division X does not appear to be critical. This fact has been considered to be the main justification for the present analysis and for not attempting to account for the rf field inhomogeneity more directly. This omission, however, may have the tendency of boosting ξ_H towards higher values in the low-pressure regime, as can be guessed by comparing the signals (b) and (c) in Fig. 9. In fact, the data measured by Paalanen *et al.*[40] in a parallel plate geometry at 0 and 10 bar fall below our ξ_H values, as indicated in Fig. 13: at 0 bar the difference is 30% or less, while at 10 bar it has dropped to less than 8%. Doubling the magnetic field to 57 mT yields slightly lower values for $\xi_H H$: at 0.5 bar and $0.6T_c$, the drop is about 6%.

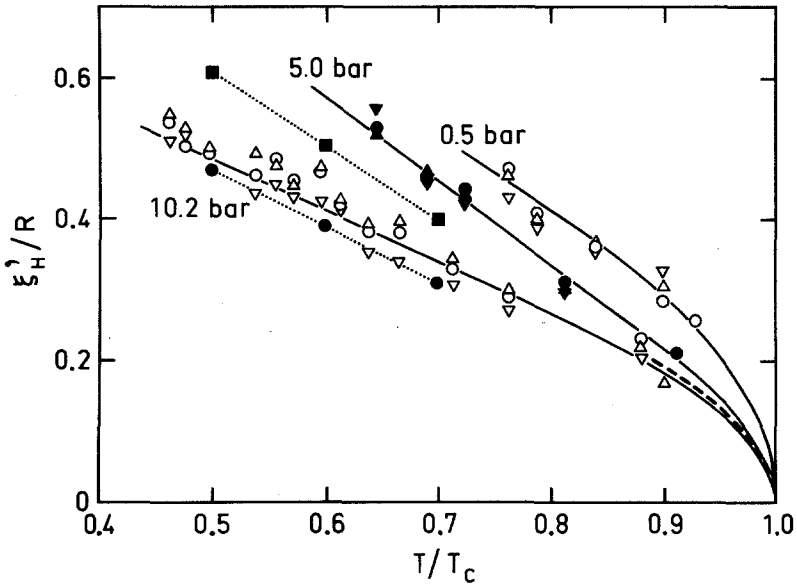

Fig. 13. Isobars of the normalized magnetic healing length $\xi'_H/R = (16/13)^{1/2}\xi_H/R$ vs. temperature at three pressures ($R = 2.5$ mm, $H = 28.4$ mT). The different choices for the division point X, as defined in Fig. 12, have been marked as follows: ($\triangle$) $X = 0.4$; ($\bigcirc$) $X = 0.5$; (∇) $X = 0.6$. The curves are fits to the data with Eq. (41) and the coefficients in Table II. The dashed curve represents the results from Ref. 41 measured at 2.72 bar. The filled squares are the 0 bar and the filled circles the 10 bar measurements from Ref. 40.

As evident from Fig. 13, below $0.9T_c$ ξ_H settles down on a near linear temperature dependence and this, in fact, is the temperature region where our analysis becomes tractable. Above $0.9T_c$ $\xi_H(T)$ is governed by a square root law such that the overall temperature dependence can be expressed in the form

$$\xi'_H/R = c_1\left(\frac{1-T/T_c}{1-c_2(1-T/T_c)}\right)^{1/2} \tag{41}$$

where c_1 and c_2 are parameters to be determined by least squares fits to the data. By means of such fitted curves, our results can be compared to the high-temperature measurements of Spencer and Ihas[41], performed at 2.72 bar in a cylindrical geometry and shown in Fig. 13 as the dashed curve. At $0.9T_c$ their result falls more than 30% below what one would interpolate from our data for a pressure of 2.72 bar. The pressure dependence of the ξ'_H isotherm at $0.75T_c$ is shown in Fig. 14 where the high-pressure end has been fixed to Osheroff's measurement[17] at the melting pressure in the temperature range 0.42–$0.75T_c$. The fitted values of the parameters c_1 and

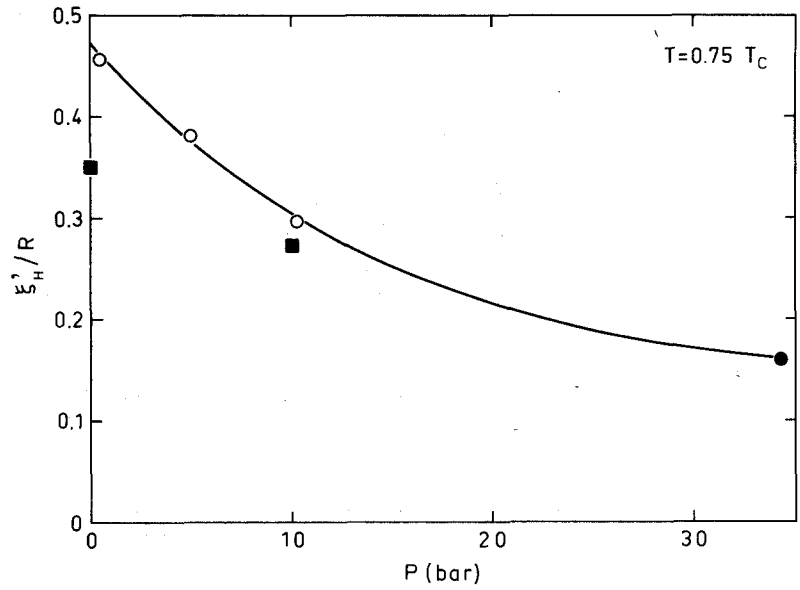

Fig. 14. Isotherm of the normalized magnetic healing length ξ'_H/R at $0.75T_c$ as a function of pressure: open circles, present measurements; filled circle, Ref. 17; filled squares, Ref. 40.

c_2 have been listed in Table II; values at other pressure can be obtained by interpolating with the help of isotherms such as the one in Fig. 14.

Finally, we conclude this subsection with the pressure dependence of ξ_H which can be used to estimate the strong coupling corrections to the β-parameter combination $\beta_{345} \equiv \beta_3 + \beta_4 + \beta_5$ where β_i are the coefficients of the fourth order free energy invariants. The bending stiffness coefficient

TABLE II

P/bar	c_1	c_2	Ref.
0	0.60	~1.0	40
0.5	0.92	0.05	This work
2.7	0.58	0.63	41
5.0	0.64	1.26	This work
10	0.47	~1.0	40
10.2	0.56	0.60	This work
34.4	0.29	0.85	17

Magnetic healing length ξ'_H/R: fitted values of the parameters c_1 and c_2 in Eq. (41) at different pressures in a magnetic field of 28.4 mT. The curves in Fig. 13 depict the fitted ξ'_H/R.

c, introduced in connection with Eq. (28), has the form[17]

$$c = \frac{13}{64}\frac{\hbar^2}{m^*}[1 - Y(T)]\frac{\rho}{m} \tag{42}$$

where m^* is the quasiparticle effective mass and ρ the liquid density. The last factor ρ/m has been included to convert from energy per atom to energy per unit volume. Close to T_c we write $1 - Y(T) \propto (\Delta/k_B T_c)^2 \propto (1 - T/T_c)\Delta C/C_>$. The magnetic anisotropy parameter a, introduced in Eq. (8), is expressed as[42]

$$a = \frac{\omega_L^2 \chi_B(\chi_N - \chi_B)}{24\gamma^2\Delta^4\beta_{345}} \tag{43}$$

By taking into account the pressure dependences[43] $\chi_N - \chi_B \propto \chi_N(\Delta/T_c)^2/(1+F_0^a)$ and $\beta_{345}^{\mathrm{BCS}} \propto \chi_N(1+F_0^a)/T_c^2$, we can finally write for the pressure dependence of $\xi_H H = (c/a)^{1/2}$ at $T \to T_c$

$$\xi_H \propto \left[\frac{\rho T_c^2 \beta_{345}}{m^* \chi_N \omega_c^2 \beta_{345}^{\mathrm{BCS}}}\right]^{1/2}(1+F_0^a)\frac{\Delta C}{C_>}(1 - T/T_c)^{1/2}\frac{1}{H} \tag{44}$$

Here $\omega_c^2 = \omega_L^2/(1 - T/T_c)$. Using Greywall's values[39] for m^* and F_0^a and Wheatley's tables[44] for ρ and χ_N, we conclude that within $\pm 10\%$ $(\beta_{345}/\beta_{345}^{\mathrm{BCS}}) \cdot (\Delta C/C_>)^2$ turns out to be a constant with pressure. The same result can be obtained by using values for β_{345} calculated by Sauls and Serene[45] and the measured $\Delta C/C_>$.[37-39]

3.4. Dipolar Coherence Length

In the spin wave equation (34), the length scale is set by the dipolar coherence length $\xi_D = (65/32)^{1/2} c_\perp/\omega_L$. In the harmonic approximation, the frequency spacing of the resonance modes is simply proportional to ξ_D and to the slope β_1 of the polar angle $\beta(r)$ in the center of the flare-out texture. Experimentally, the spacing is found to follow accurately the harmonic spectrum and thus the dipolar length can be read directly from the measured signals once the magnetic healing length $\xi_H(P, T)$ is known and the flare-out texture thereby becomes fixed (cf. Fig. 7).

The results for ξ_D from the stationary state measurements, based primarily on the two lowest eigenfrequencies (cf. Fig. 19), are shown in Fig. 15 as a function of temperature at four different pressures. In Fig. 16 ξ_D is plotted as a function of pressure at a temperature of 0.63–$0.64\,T_c$. In this figure the solid line gives the pressure dependence of $\xi_D \propto [\rho[1 - Y(T)]/(m^* \chi_B \omega_L^2)]^{1/2}$, where the gap renormalization in $Y(T)$, important close to T_c, is not included. The curve has been adjusted to $\mu_D = 9\,\mu$m at 30 bar for a best fit. This choice for the high pressure value of ξ_D agrees within 10% with Osheroff's measurements of the spin-wave velocity $c_\perp = \sqrt{2}\, c_\parallel 17 = (32/65)^{1/2}\, \omega_L \xi_D$ at the melting pressure.

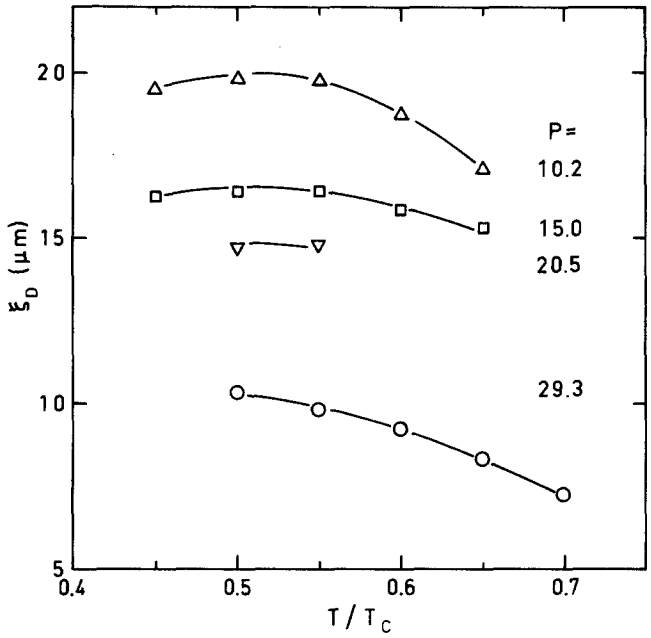

Fig. 15. Dipolar coherence length ξ_D, determined from a comparison of the measured and calculated spacing of the spin-wave resonance modes, plotted as a function of temperature at different pressures.

The values obtained here for ξ_D depend sensitively on what values are used for ξ_H in the data analysis, in particular at low pressures. If we use for ξ_H the values measured by Paalanen *et al.*,[40] for instance, then ξ_D has to be increased from 34 μm to 44 μm at 0.5 bar while at 10 bar the required increase drops to 10%. We estimate that the overall uncertainty in our ξ_D values is about 15%.

It is interesting to note that the ratio ξ_D/ξ_H determines the basic textural anisotropy parameter a, defined in Eq. (8), which is used as scaling parameter for the textural energies, as expressed, e.g., in Eqs. (30). Thus one obtains

$$a = \frac{1}{2}\chi_B \left(\frac{\omega_L \xi_D}{\omega_0 \xi_H}\right)^2$$

The parameter a is sometimes also written in terms of an effective g-value shift[17]

$$a = \frac{5}{4}\chi_B \frac{\Delta g}{g}$$

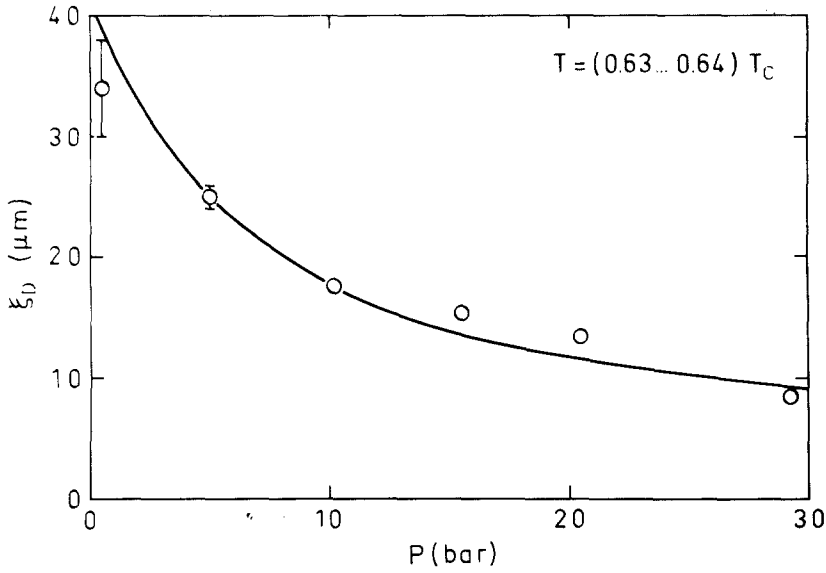

Fig. 16. Dipolar coherence length ξ_D, determined from the measured frequency spacing of the spin-wave resonance maxima, plotted as a function of pressure at 0.63–$0.64\,T_c$. The solid line represents the theoretical pressure dependence, adjusted to $\xi_D = 9\,\mu$m at 30 bar. The error bars illustrate the experimental uncertainty in determining the spacing of the spin-wave peaks.

Our analysis of the stationary state spectra gives ξ_D and ξ_H as a function of temperature at one common pressure, namely 10.2 bar. Taking the ratio of the data presented in Figs. 13 and 15, we find that $\Delta g/g$ varies from $5.2 \cdot 10^{-6}$ at $0.44\,T_c$ through a shallow maximum of $6.0 \cdot 10^{-6}$ at $0.54\,T_c$ to $4.6 \cdot 10^{-6}$ at $0.66\,T_c$. These values agree with the magnitude of Osheroff's measurements at melting pressure[17] but not in the sign of the curvature of the $\Delta g/g$ curve with respect to temperature.

3.5. Spin Diffusion

On a phenomenological level, spin diffusion is incorporated in the spin-wave equation (34) with the additional term $(i/2\pi)\nu D\nabla^2 S_+$. A perturbation expansion with neglect of all off-diagonal elements then gives for the eigenfrequencies instead of Eq. (37)

$$E_n + i\Gamma_n = [2\sqrt{f}\,\xi_D\beta_1 + iD\nu_0\beta_1/(\pi\sqrt{f}\,\xi_D\nu_L^2](n+1) \qquad (45)$$

where $f = 48/65$. The parameter which determines the decay of the amplitude of the resonances is the ratio of the energy to the width of the mode $E/2\Gamma = \pi f\xi_D^2\nu_L^2/(\nu_0 D)$. An effective spin diffusion constant can thus simply

be determined by comparing the measured spin-wave spectra to a superposition of equally spaced lines with linewidths increasing as $2(n+1)\beta_1 D/(2\pi\xi_D\sqrt{f})$ in units of frequency, as shown in Fig. 8 for two different ratios of E/Γ. This analysis suffers from the unaccounted line broadening due to magnetic field inhomogeneities but, nevertheless, the measured and the simulated reference spectra seem to agree well with each other.

At 29.3 bar in the temperature range 0.55–$0.70T_c$, the effective spin diffusion is found to be roughly constant with a value $D_{\text{eff}} = 2.2 \cdot 10^{-2}\,\text{cm}^2/\text{sec}$. This result is obtained with $\xi_D = 9\,\mu\text{m}$. At 10.2 bar with $\xi_D = 19\,\mu\text{m}$ the analysis gives $D_{\text{eff}} = 2.2 \cdot 10^{-2}\,\text{cm}^2/\text{sec}$ at $0.50T_c$, $4.5 \cdot 10^{-2}\,\text{cm}^2/\text{sec}$ at $0.54T_c$ and $7.5 \cdot 10^{-2}\,\text{cm}^2/\text{sec}$ at $0.60T_c$. These values for the spin diffusion coefficient in ^{3}He-B are of the same order of magnitude as in the normal phase at T_c for which Brewer *et al.* give $D(T_c) = 11 \cdot 10^{-2}\,\text{cm}^2/\text{sec}$ at 10 bar and $D(T_c) = 2.4 \cdot 10^{-2}\,\text{cm}^2/\text{sec}$ at 29 bar.[46] Qualitatively, the results display the experimental observation that the spin-wave modes become more and more visible with decreasing temperature, i.e., as D_{eff} decreases. This feature has also been observed by Candela *et al.*[47] who have studied standing spin waves localized in a magnetic field gradient to the vicinity of a confining wall.

4. RESULTS IN THE ROTATING STATE

4.1. Introduction

In uniform rotation at constant angular velocity Ω, the equilibrium state of the flare-out texture is modified by the appearance of a lattice of singly quantized rectilinear vortices. This orienting effect, which because of the long-range magnetic coherence is averaged out over the vortex lattice, produces an additional tilt of the anisotropy axis $\hat{\mathbf{n}}$ from the central axis of the flare-out texture. It is controlled by the textural parameters λ and κ which were introduced in Eq. (25) and, via the vortex density $n_v = 4m\Omega/h$, are directly proportional to Ω. These parameters reflect the structure of the rectilinear vortices and today, with the advent of the solutions for the two B-phase vortex structures, they can be calculated in qualitative agreement with experiment.[9,22]

Figure 17 summarizes our calculations on the orienting effect of rotation on the flare-out texture by showing quantitatively the dependence of the polar angle β as a function of the reduced radius r/R on the value of λ. As long as all other textural parameters controlling the flare-out texture are known from the analysis of the stationary state measurements as a function of temperature and pressure, the graphs in Figs. 17a–f can be used to determine the values of the rotation dependent textural parameters by

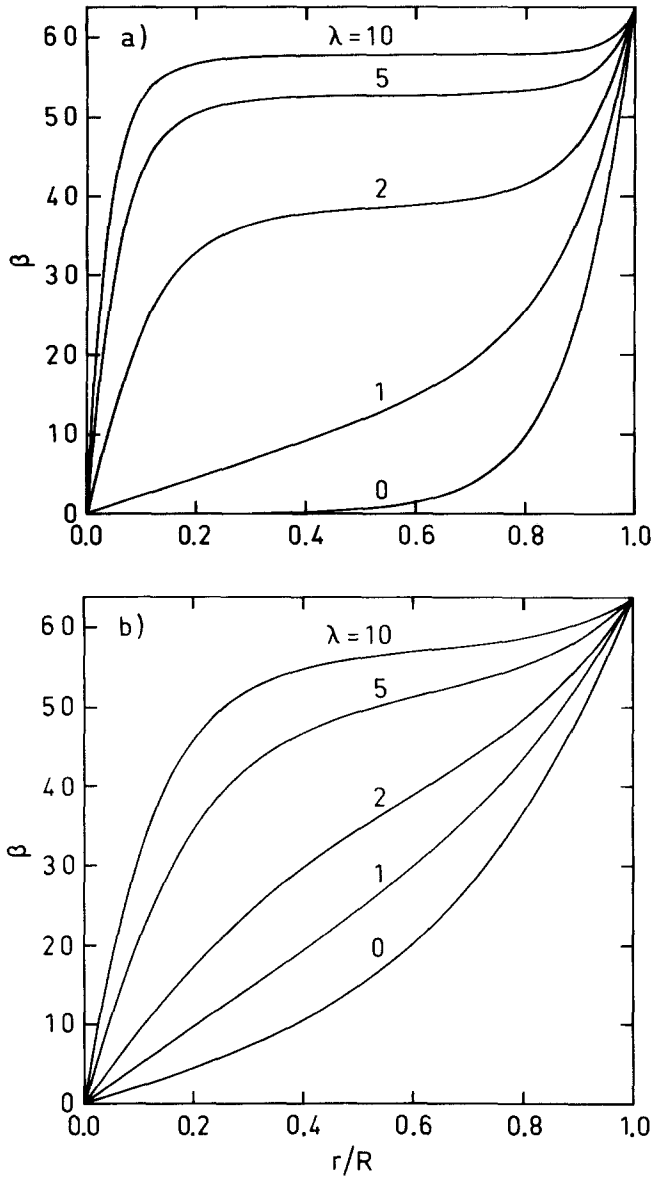

Fig. 17. The effect of rotation on the flare-out texture. In (a)–(c), the polar angle β (in degrees) is plotted vs. the normalized radial distance r/R at different values of the vortex free energy parameter λ and the magnetic healing length ξ'_H: (a) $\xi'_H/R = 0.1$; (b) $\xi'_H/R = 0.3$; (c) $\xi'_H/R = 0.5$. In figures (d)–(f), the corresponding local oscillator spectra are shown with the resonance absorption plotted vs. the scaled frequency shift. The stationary state curves ($\lambda = 0$) can also be seen in Figs. 3 and 4 in a more compact presentation.

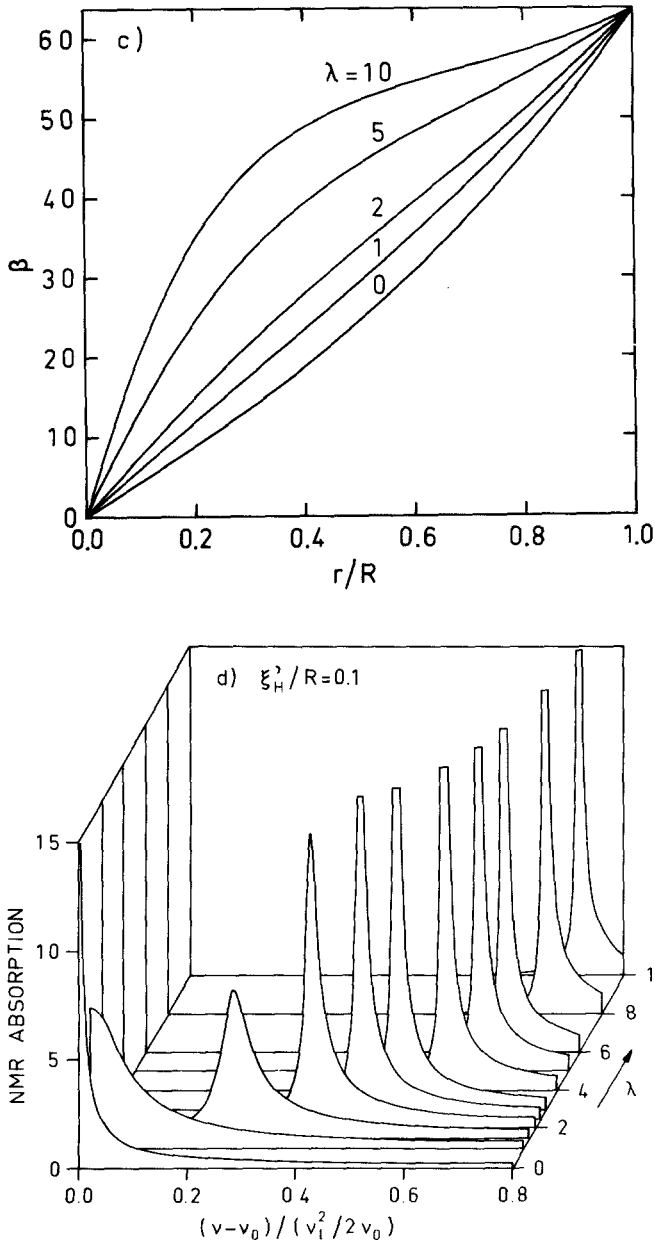

Fig. 17. Continued

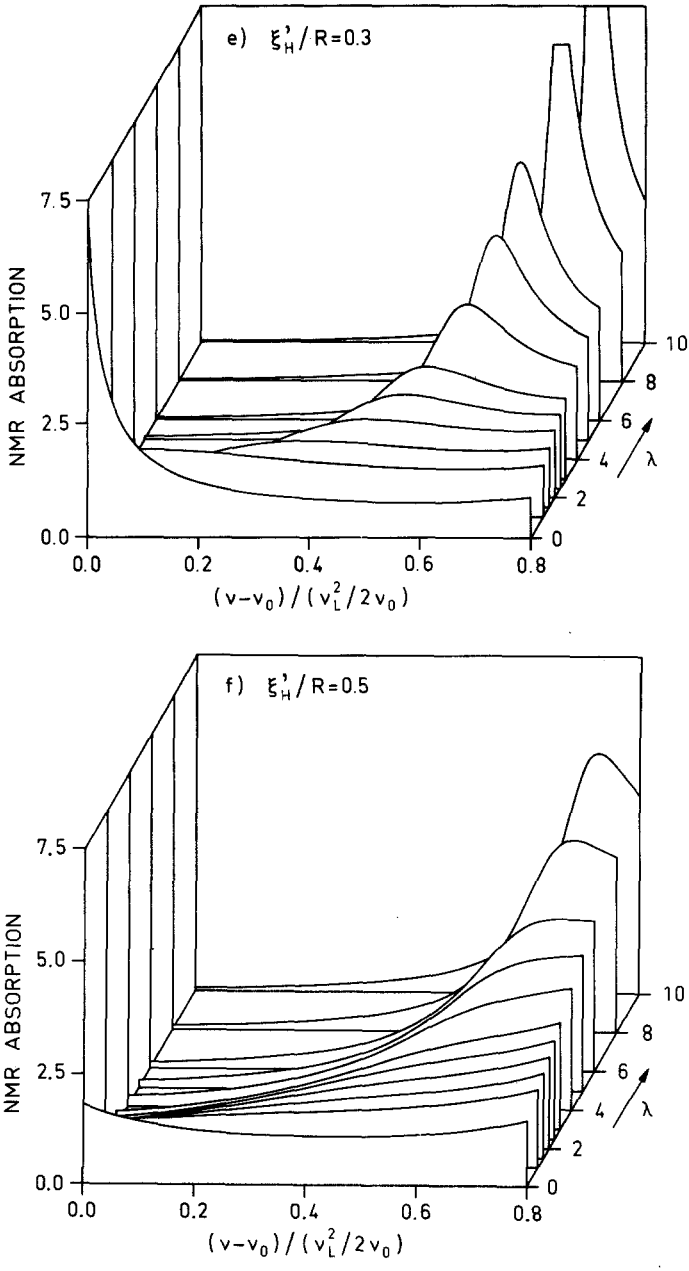

Fig. 17. Continued

comparing the plots with the experimental results. In this context it is useful to note that in an axial magnetic field the gyromagnetic contribution F_{gm}, as defined in Eq. (24), is of similar form as the magnetic orientational energy in Eq. (8). Thus the modifications in the texture due to κ/H can be obtained by simply incorporating them as a renormalization of ξ_H to $\xi_H/(1\pm\kappa/H)^{1/2}$ and of λ to $\lambda/(1\pm\kappa/H)$. Accordingly the plots in Fig. 17 are sufficient for evaluating the rotation induced changes in the flare-out texture. The general feature characterizing the NMR properties is illustrated in Figs. 17d–f, which show the resonance absorption calculated in the local oscillator approximation: with increasing Ω, more and more of the absorption is piled towards the high-frequency end of the NMR absorption region. In particular, at high rotation speeds, a plateau in the β vs. r plots of Figs. 17a–c is seen to emerge, corresponding to a bulk-liquid-like orientation, which in the resonance absorption curves of Figs. 17d–f produces a distinct absorption maximum.

Three different alternative methods have been employed for analyzing the rotating state spectra. 1) At high pressures 10.2 bar $\leq P \leq$ 29.3 bar the spacing of the spin-wave resonance absorption peaks yields directly the slope β_1 of the polar angle $\beta = \beta_1 r$ in the center of the flare-out texture which then allows one to read the corresponding interpolated λ value from the graphs in Fig. 17. At low pressures the spin-wave resonance modes are not sufficiently well resolved, owing to their smaller frequency spacing when $\nu_L(P, T)$ decreases with decreasing pressure. The homogeneity of the polarizing field is limited to $\Delta H/H \sim 4 \cdot 10^{-5}$ and thus the smallest observable spin-wave spacing is of the order of 40 Hz at a resonance frequency $\nu_0 \simeq 1$ MHz. Consequently, similar to the stationary state measurements, at low pressures 0.5 bar $\leq P \leq$ 10.2 bar one has to resort to the line shape analysis based on the local oscillator model. This has been done using one of two alternative methods. 2) The ratio of the integrated NMR absorptions under the low- and high-frequency portions of the measured signal envelopes can be used as a measuring stick to determine λ in much the same manner as ξ_H was determined in Sec. 3.3 from the stationary state results. 3) One can also use the frequency shift of the absorption maximum with bulk-liquid-like properties for determining λ from Eq. (26). In the overlap cases, where two of the different data analysis techniques have been used and can be compared, good agreement is generally found.

4.2. Spin-Wave Resonance Absorption

As shown in the inset of Fig. 19a, the spin-wave absorption peaks move further apart with increasing rotation speed. The computed dependence of the spin-wave modes on rotation via the λ parameter has been compiled

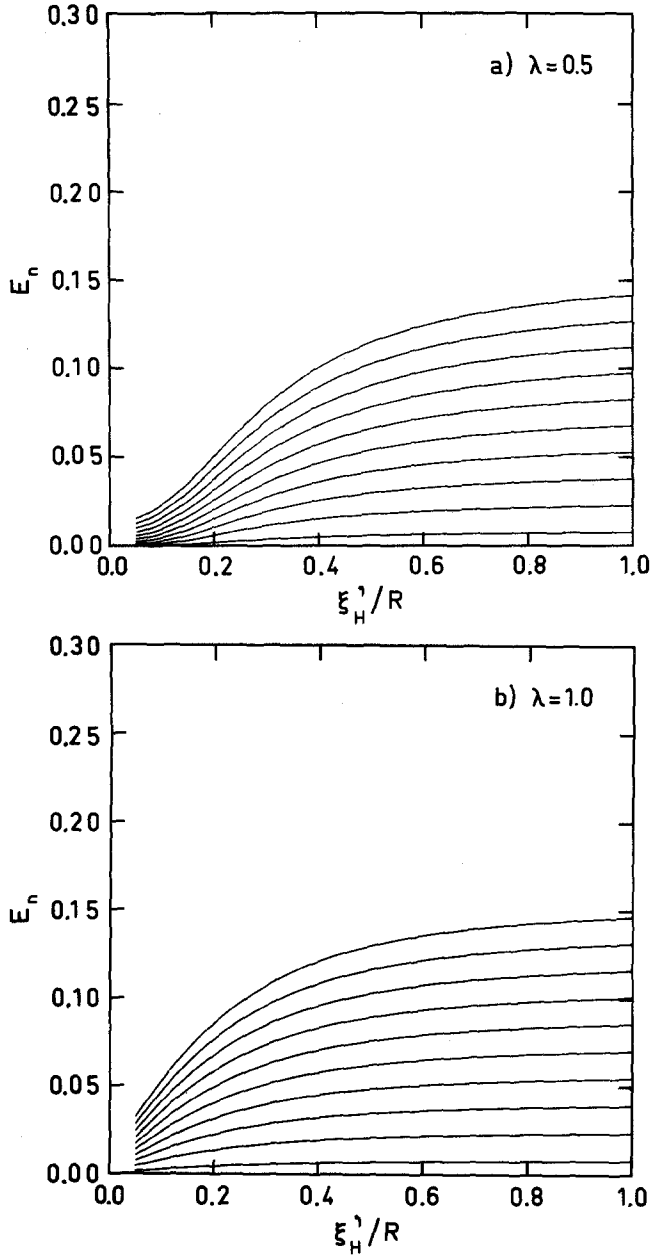

Fig. 18. Calculated spin-wave resonance spectra in the rotating state, expressed in the dimensionless form of Eq. (37), plotted as a function of the normalized magnetic healing length ξ'_H/R. The corresponding spectrum for the stationary state is shown in Fig. 7. The dipole length $\xi_D = 10\,\mu$m. The textural transition described by Eq. (26) is seen as an abrupt change in the $R \to \infty$ asymptotes of the E_n, when λ exceeds 1.

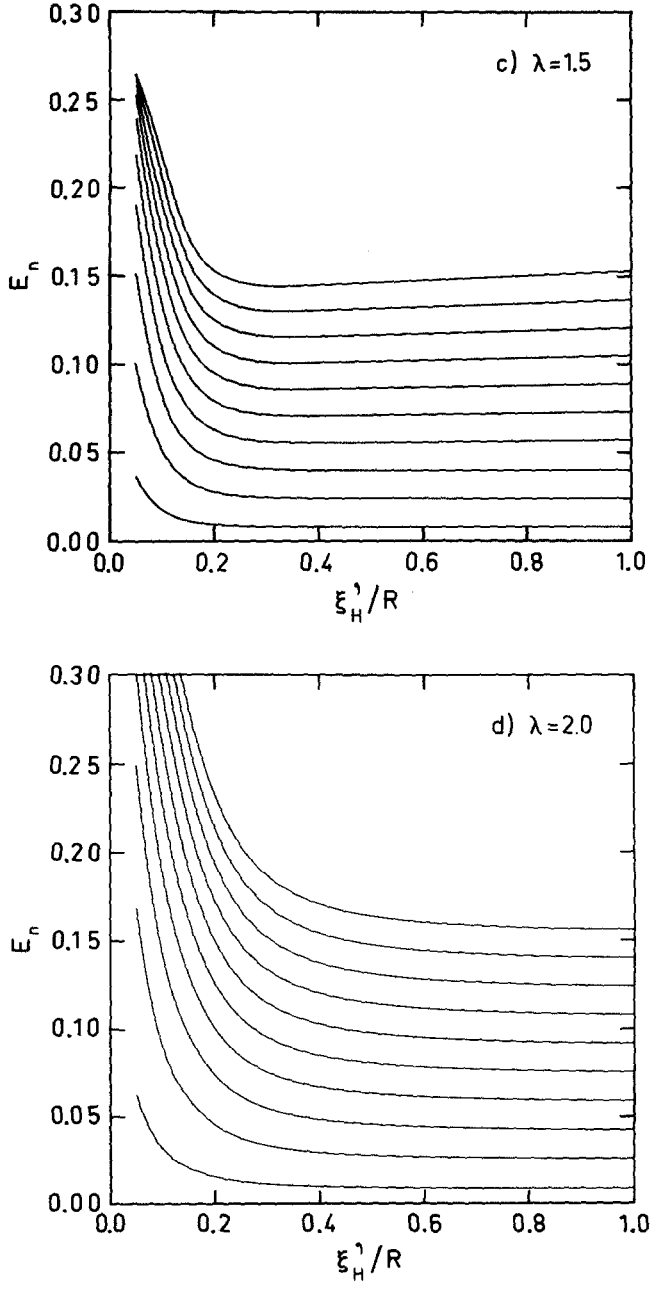

Fig. 18. Continued

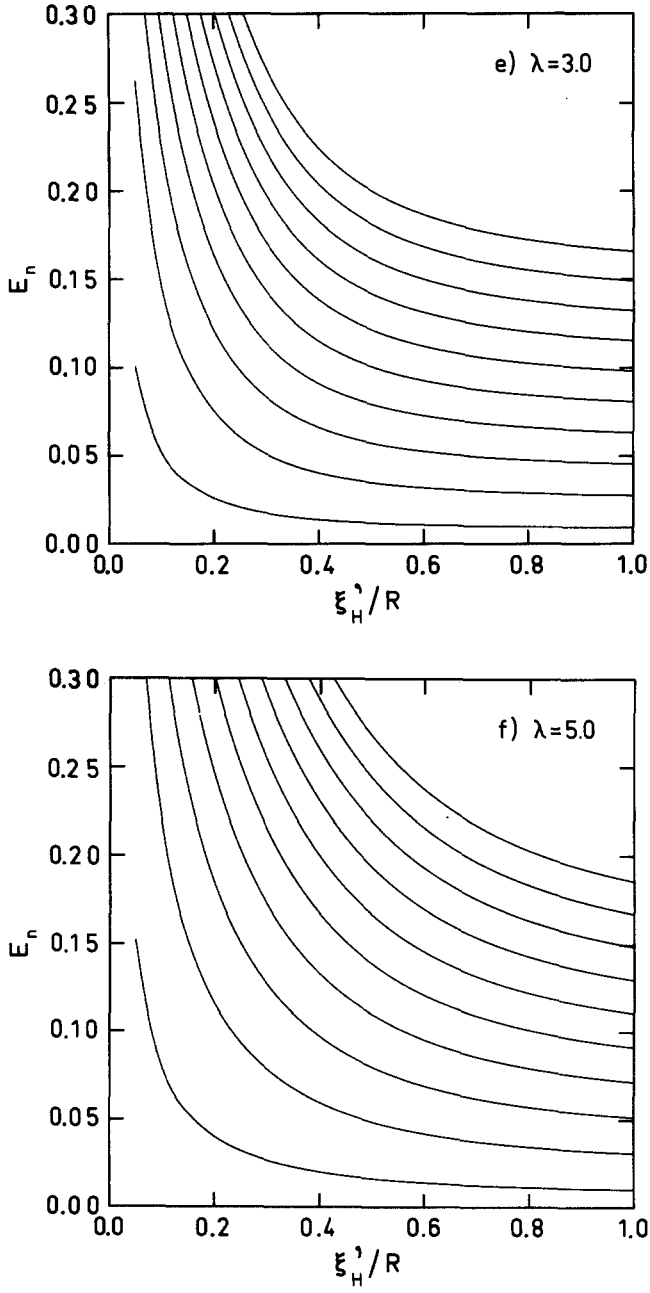

Fig. 18. Continued

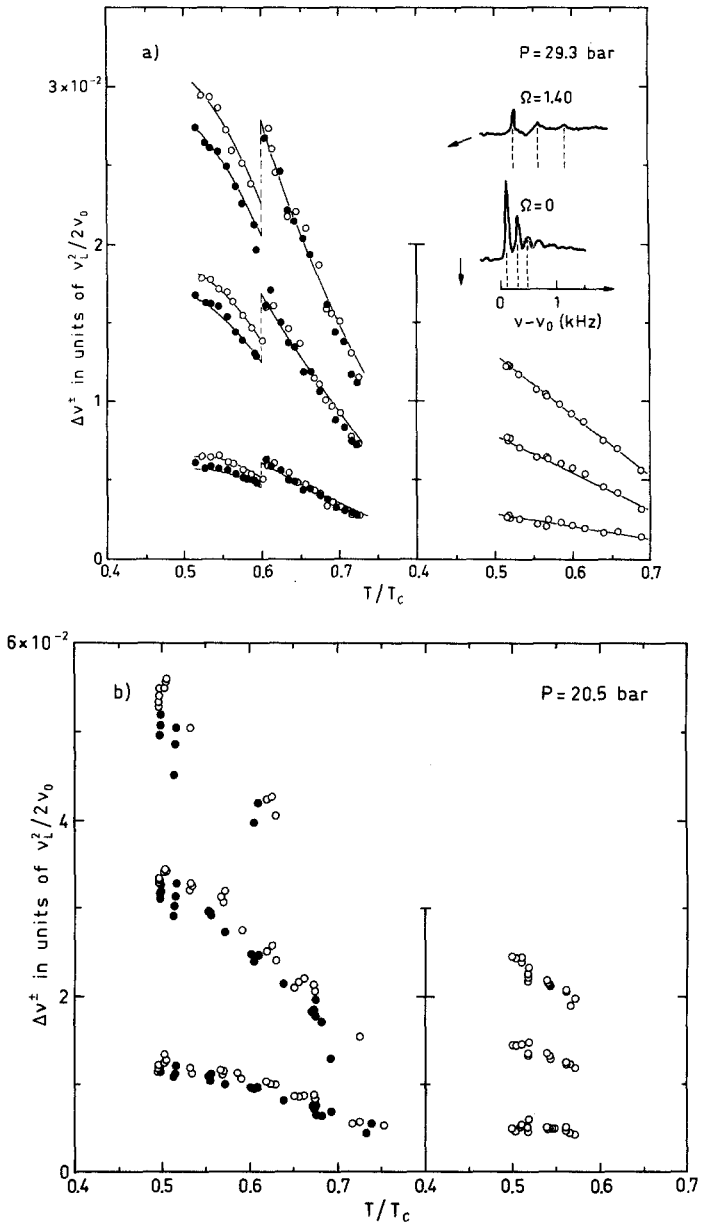

Fig. 19. Measured frequency shifts $\nu_n^+ - \nu_0$ and $\nu_n^- - \nu_0$ of the first three spin-wave resonance absorption peaks ($\nu_0 = 922.5$ kHz): open circles, $\nu_n^+ - \nu_0$ with $\mathbf{\Omega}\uparrow\uparrow\mathbf{H}$; filled circles, $\nu_n^- - \nu_0$ with $\mathbf{\Omega}\downarrow\uparrow\mathbf{H}$. The rotation velocity is $\mathbf{\Omega} =$ 1.40 rad/sec in the left half while the right half represents the stationary state in each of the figures (a)-(d). The solid curves in (a) show the final fit to the measurements, while the inset illustrates the low-frequency part of the NMR absorption signal with the spin-wave resonance peaks, measured at $T/T_c =$ 0.51 in both the rotating and stationary states.

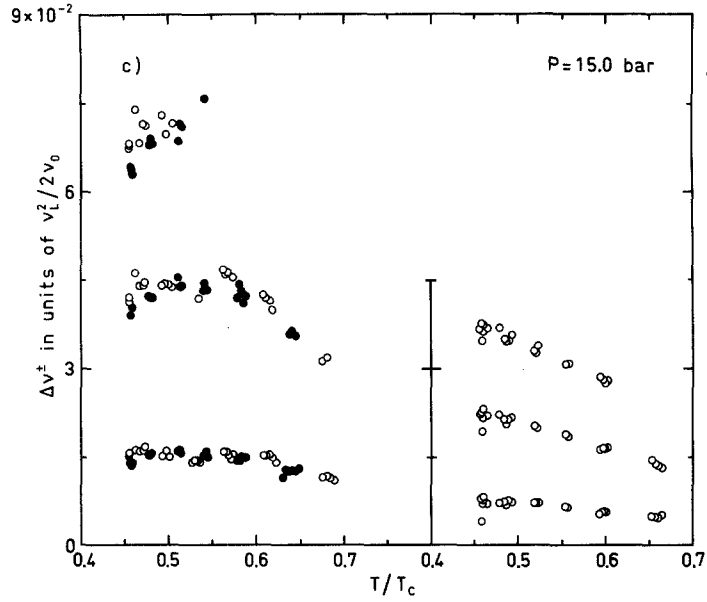

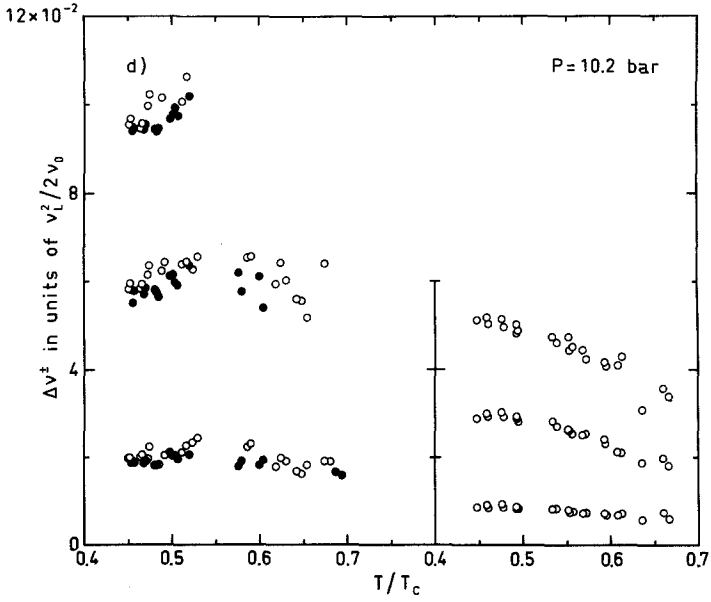

Fig. 19. Continued

in Figs. 18a-f. In these six figures, the ten lowest eigenvalues E_n have been plotted as a function of ξ_H for six different values of λ. From these graphs it can be seen that if ξ'_H/R and λ fall in the intervals $0.2 < \xi'_H/R < 0.5$ and $0 < \lambda < 2.5$ then the spin-wave spectra are expected to yield λ with reasonable resolution. These are, in fact, the appropriate ranges of variation for ξ'_H/R and λ in the present experiments at pressures above 10 bar and in a field of 28.4 mT.

In Fig. 19 the measured frequency shifts of the three lowest spin-wave absorption peaks have been plotted as a function of temperature, with the stationary state results on the right-hand side and the rotating data, obtained with $\Omega = 1.4$ rad/sec, on the left. Forward rotation with $\boldsymbol{\Omega} \uparrow\uparrow \mathbf{H}$, which corresponds to a minus sign in Eq. (25), has been denoted with open circles, while filled circles apply for reverse rotation with $\Omega \downarrow\uparrow \mathbf{H}$. Since the resolution in determining the third eigenmode is often poor, the splitting between the first two modes has been used to extract ξ_D from the stationary state (see Sec. 3.4). In a similar fashion, λ has been determined from the rotating state data by fitting the averages $(\nu_n^+ + \nu_n^-)/2$. Finally, the gyromagnetic splitting can be expressed in the form

$$\frac{1}{2}(\nu_n^+ - \nu_n^-) = \frac{\kappa \xi_H}{2H} \frac{\partial E_n}{\partial \xi_H} + \frac{\lambda \kappa}{H} \frac{\partial E_n}{\partial \lambda} \tag{46}$$

since κ/H is small (~ 0.05). In this way κ/H can be determined from the gyromagnetic splitting of any mode which then fixes the whole spectrum. This splitting is of order 10 Hz at a resonance frequency of $\nu_0 \sim 1$ MHz and can be determined with desirable precision only at higher pressures at temperatures below the vortex core phase transition. In the spin-wave spectra in Fig. 19, the vortex core transition is present only at 29.3 bar, where it is prominently displayed as a remarkable discontinuity at $T = 0.60\,T_c$.

Figure 19a illustrates the compatibility of the measured and calculated eigenmodes after fitting ξ_D, λ, and κ/H at fixed temperature intervals to smoothed curves through the measured data. As explained above, for the fitting procedure, each parameter requires only one frequency splitting and thus the redundancy in the data, i.e., the presence of three eigenmodes with gyromagnetic shifts in each case, only serves to demonstrate the internal consistency of the analysis. However, to obtain this agreement, a zero shift has to be applied to E_0 which, in the normalized units of Fig. 19, appears essentially temperature-independent with a magnitude of $\Delta E_0 \sim 5 \cdot 10^{-4}$ at 29.3 bar. This corresponds to a NMR frequency shift of the superfluid resonance relative to the normal state Larmor value, a g-value shift with $\Delta g/g = 2 \cdot 10^{-5}$ at $T = 0.5\,T_c$ and $1 \cdot 10^{-5}$ at $T = 0.7\,T_c$. The order of magnitude of these g-value shifts agrees with those quoted by Osheroff[15,17] and our values at the end of Sec. 3.4.

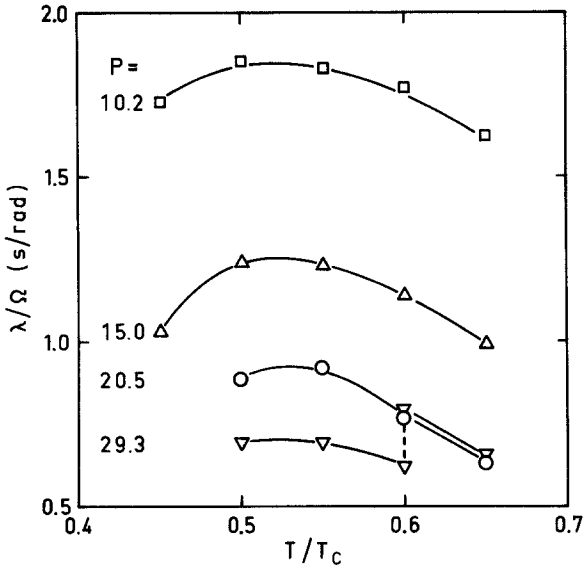

Fig. 20. The orientational free energy parameter λ at different pressures, plotted as λ/Ω (in units of sec/rad) vs. temperature. The graphs represent a summary of the fits to the spin-wave resonance absorption measurements in Figs. 19.

In Fig. 20 the λ values determined from the spin-wave spectra have been compiled as a function of temperature at different pressures. These results are in good agreement with NMR frequency shift measurements in tilted magnetic fields,[21] which can be analyzed simply on the basis of the bulk liquid behavior. In Fig. 20 the phase transition of the vortex core structure is again prominently present in the 29.3 bar data at $T=0.60T_c$. Here the discontinuity mainly reflects the change in the induced magnetizations of the two core structures. The parameter κ/H, which measures the spontaneous magnetization of the core structure, also undergoes a discontinuous change at the transition. At 29.3 bar $\kappa/(H\Omega)\sim 0.024$ below and ≤ 0.005 sec/rad above the transition temperature. Both the properties of the vortex core transition as well as more details about the determination of κ will be presented in a forthcoming report dealing with similar texture measurements in tilted magnetic fields.[48]

4.3. Line Shapes

Line shape analysis in the rotating state proceeds in much the same fashion as in the stationary case in Sec. 3.3. There the determination of the magnetic healing length ξ_H was based on a comparison of a computed

reference value with the measured result for the ratio $(I_B/I_A)_X$ of the integrated resonance absorptions in the high- and low-frequency portions of the NMR signal envelope (see Fig. 12). In the rotating case, where ξ_H is already known from the stationary state analysis, the same procedure is employed to provide a value for λ based on the computed graphs for the ratio $(I_B/I_A)_X$ as a function of ξ_H and λ, as shown in Fig. 21. The division point separating the high and low frequency parts of the signal has here been chosen to be $X = \sin^2\beta = 0.5$, although the divisions $X = 0.4$ and 0.6 have also been used in the data analysis with equivalent results.

In Fig. 22 a sequence of consecutive NMR signals is shown while the rotation speed is gradually increased from zero up to 1.4 rad/sec. These low-field ($H = 28.4$ mT) measurements have been performed at our lowest pressure of 0.5 bar with $T = 0.77\,T_c$ where $\xi_H/R \sim 0.44$. In Fig. 23 the corresponding λ values are plotted as a function of Ω. The linear dependence confirms the consistency of the data analysis and also the fact that λ depends linearly on the density of vortices in the container. Comparing the different line shapes in Fig. 22, we note that at high rotation speeds, the integration

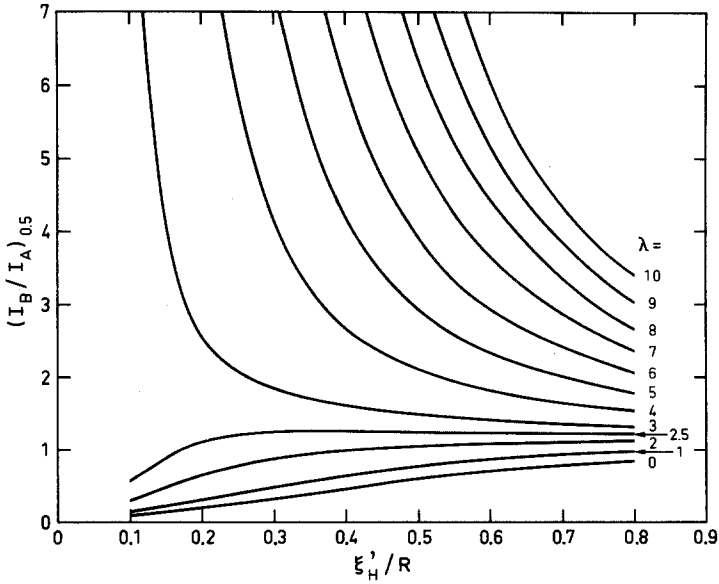

Fig. 21. Signal analysis on the basis of the intensity distribution according to the local oscillator model: the calculated ratio $(I_B/I_A)_{X=0.5}$ of the integrated resonance absorptions in the high-frequency (I_B) and low-frequency (I_A) sections of the local oscillator spectrum, shown as a function of ξ_H and λ. The graph representing the stationary state ($\lambda = 0$) is shown in expanded scale in Fig. 12.

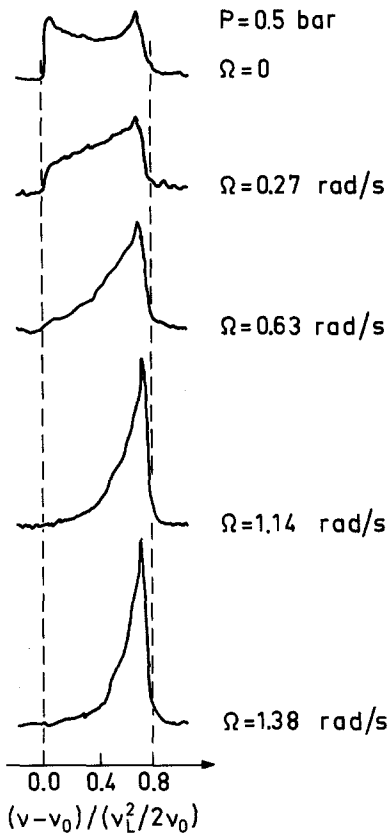

Fig. 22. NMR absorption signal envelopes at consecutively higher rotation velocities: $P = 0.5$ bar, $T = 0.77 T_c$, $H = 28.4$ mT, and $\xi'_H = 0.44R$. These signals demonstrate the changes in the NMR spectrum with increasing Ω when ξ'_H is large (in contrast to Fig. 25 where ξ'_H is small).

procedure becomes increasingly inadequate. First of all, the integrated intensity I_A in the low-frequency part decreases rapidly with increasing Ω. Secondly, at the same time, the uncertainty in fixing the relative frequency scale, i.e., in identifying the $\sin^2\beta = 0.8$ absorption edge and the corresponding division point X, becomes critical. The second problem can be removed by choosing $\sin^2\beta = 0.8$ such that the determination of λ becomes independent of the choice for X. The final result in Fig. 23 appears satisfactory, perhaps fortuitously, but also because the diverging character of the constant λ curves at high Ω in Fig. 21 compensates for the increased scatter in $(I_B/I_A)_X$.

Unlike in the A-phase, a critical rotation velocity for the formation of vortices is not clearly observable in Fig. 23. This is due to the fact that basically the B-phase NMR signal identifies the presence of vortices via their influence on the texture and thus monitors the vortex density whereas in the A-phase it is directly the number of vortices which adds up in the

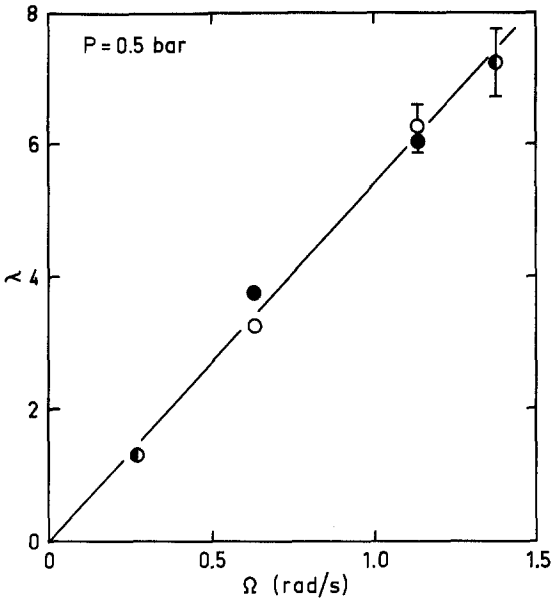

Fig. 23. The vortex susceptibility parameter λ as a function of rotation velocity Ω as determined from the line shapes in Fig. 22 using the graphs in Fig. 21. The open circles correspond to forward rotation ($\mathbf{\Omega}\uparrow\uparrow\mathbf{H}$) at $0.77\,T_c$, while the filled circles represent reverse rotation ($\mathbf{\Omega}\downarrow\uparrow\mathbf{H}$) at $0.76\,T_c$.

intensity of a satellite NMR absorption peak.[30] The counter flow current, originating from a deficit of vortices, is located in a narrow sliver next to the container wall and is too weak to cause any observable changes in the B-phase NMR line shapes in this context.[19]

In Fig. 24 λ/Ω is shown as function of temperature at 5.0 and 10.2 bar pressures, as deduced using the line shape analysis. The 10.2 bar data agree within 15% with the results obtained from the spacing of the spin-wave absorption peaks (cf. Fig. 20) and similarly with measurements in inclined magnetic fields[48] which are represented by the dashed line. At 5.0 bar the frequency shift of the main absorption line can be used to measure λ close to T_c where ξ_H is still small and the Ω-dependent absorption peak can be monitored (cf. Sec. 4.4.). As expected, these λ values are also in good agreement with those derived from the line shape analysis.

Finally, we may note from Fig. 24 that within the scatter of the data, the gyromagnetic shift is only barely distinguishable at low pressures. However, the 5.0 bar measurements point to the fact that on approaching T_c, κ remains finite and appears to reach at T_c the value $\kappa/\Omega \sim 0.7\,\mathrm{mT}\cdot\mathrm{sec/rad}$.

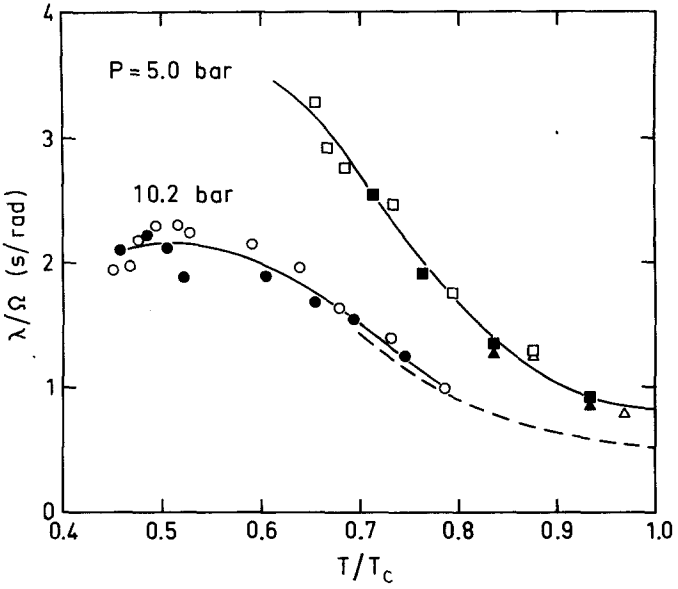

Fig. 24. λ/Ω as a function of T/T_c, as determined from the line shape analysis; squares, $P = 5.0$ bar and $\Omega = 1.7$ rad/sec; circles, $P = 10.2$ bar and $\Omega = 1.4$ rad/sec. Open symbols refer to forward and filled ones to reverse rotation. The magnetic field is 28.4 mT. At 5.0 bar λ has also been determined from the bulk-liquid-like frequency shift of the main absorption maximum (triangles). The dashed curve at 10.2 bar represents measurements in a magnetic field tilted from the axial orientation, analyzed assuming bulk-liquid-like behavior (cf. Ref. 48).

4.4. Frequency Shift of the Main Absorption Maximum

When ξ_H is small, the central region of the flare-out texture acquires bulk-liquid-like textural properties during rotation. These features are illustrated in Fig. 25 by a sequence of successive NMR absorption signals at consecutively higher rotation velocities. The measurement has been performed at high pressure ($P = 25.0$ bar) and in relatively high magnetic field ($H = 50$ mT) such that the magnetic healing length remains small ($\xi'_H = 0.15$ R) even at low temperatures ($T = 0.57\,T_c$). The NMR signal displays a prominent maximum which in the stationary state borders to the Larmor edge. With increasing Ω the peak is broadened and shifted to higher frequencies, at first only barely but above a critical angular velocity of $\Omega_c \sim 1.3$ rad/sec more rapidly. This peak corresponds to the plateau in the $\beta(r)$ curves of Fig. 17a at large values of λ, and its frequency shift is approximately given by the bulk liquid expression in Eq. (26). In Fig. 26 the scaled frequency shift $\Delta\nu/[\nu_L^2/(2\nu_0)]$ is plotted as a function of Ω. The

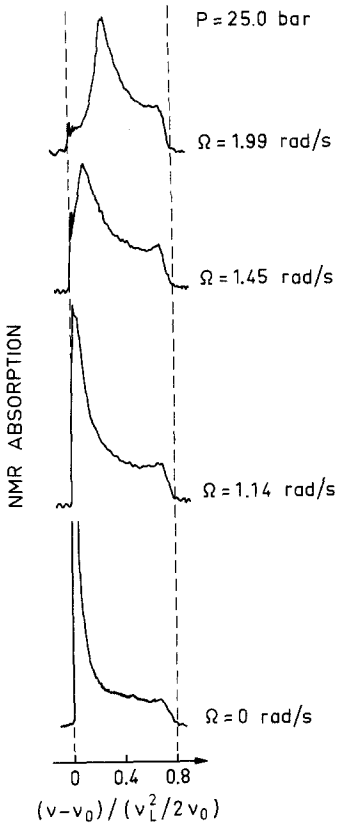

Fig. 25. NMR absorption signal envelopes at different rotation velocities demonstrating the increasing frequency shift of the main absorption maximum with increasing Ω: $P = 25.0$ bar, $T = 0.57 T_c$, $H = 50$ mT, and $\xi'_H = 0.15$ R.

solid line corresponds to the bulk liquid behavior in accordance with Eq. (26). The measurements fall on the dashed line which has a more gradual dependence on Ω, in particular in the vicinity of the critical velocity Ω_c where λ passes through the value $\lambda = 1$. Clearly the finite size of the container and the influence from the wall orientation affect the texture in the central region at low velocities but, with increasing Ω, Eq. (26) is obeyed with improved precision. At high Ω and small ξ_H/R, the bulk-liquid-like frequency shift of the main NMR absorption maximum thus provides a straightforward means of determining λ, independently of any prior knowledge of ξ_H or ξ_D.

An example of the bulk-liquid-like frequency shift analysis is shown in Figs. 27 and 28. In the former the scaled values of the frequency shifts $\Delta\nu^+$ and $\Delta\nu^-$ have been plotted as a function of temperature, measured at a rotation velocity of $\Omega = 2.0$ rad/sec. In Fig. 28 the results have been

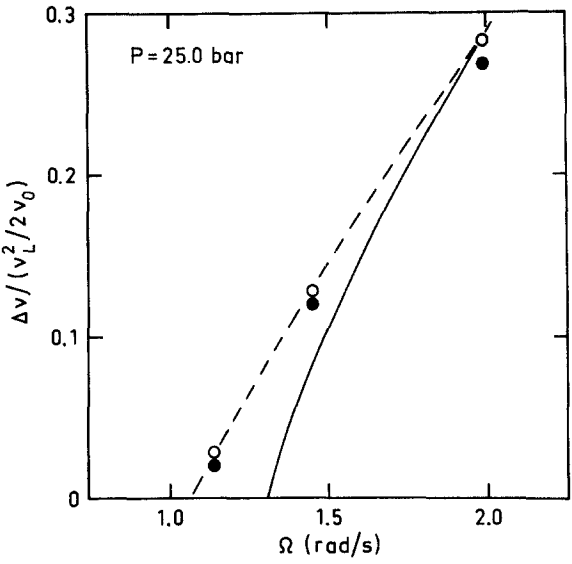

Fig. 26. The frequency shifts $\Delta\nu^{\pm}$ of the main absorption maximum, extracted from the signals in Fig. 25 and plotted as a function of the rotation velocity Ω while the cryostat is decelerated ($d\Omega/dt<0$): open circles, forward rotation ($\mathbf{\Omega}\uparrow\uparrow\mathbf{H}$) at $T=0.58T_c$; filled circles, reverse rotation ($\mathbf{\Omega}\uparrow\downarrow\mathbf{H}$) at $T=0.56T_c$. The solid curve represents the bulk liquid shift $\nu^+-\nu_0$ according to Eq. (26) with $\lambda/\Omega=0.748$ sec/rad and $\kappa/(H\Omega)=0.016$ sec/rad, obtained by adjusting Eq. (26) to the measured shifts at $\Omega=1.99$ rad/sec. The dashed line depicts the observed behavior in the presence of the orientational influence from the walls of the sample container.

converted to values of λ/Ω using Eq. (26). The second-order nature of the textural transition at $\lambda=1$ is experimentally very obvious at low temperatures where the frequency shift of the main absorption maximum suddenly appears as λ increases steeply and exceeds 1 at about $0.3T_c$ (see Fig. 27).

To illustrate the general properties of $\lambda(T)$, Fig. 28 has been supplemented with additional data from measurements in a field of likewise 56.9 mT but now oriented at an angle $\mu=25°$ with respect to the axial direction. This situation can similarly be dexterously analyzed on the basis of bulk-liquid-like behavior and, moreover, over a wider range since the restriction $\lambda>1$ does not apply. The general form of the $\lambda(T)/\Omega$ curve in Fig. 28 closely resembles the calculated λ contribution from Fig. 2. This figure allows one to gauge the approximate magnitudes of its two components, the intracore contribution λ_c and the superflow term λ_f. Clearly at temperatures below $0.3T_c$, λ_f is vanishingly small such that the measured

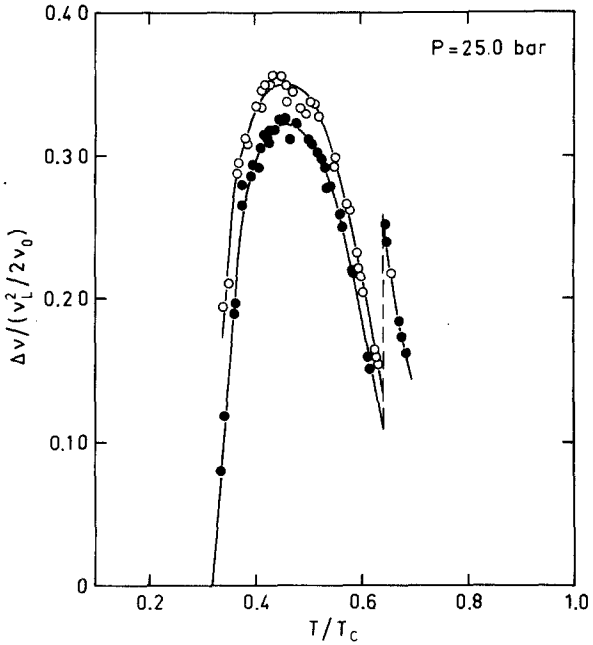

Fig. 27. Temperature dependence of the frequency shifts $\nu^+ - \nu_0$ (open circles) and $\nu^- - \nu_0$ (filled circles) for the main absorption maximum: $P = 25.0$ bar, $H = 56.9$ mT (i.e., $\nu_0 = 1845$ kHz), and $\Omega = 2.0$ rad/sec.

value of λ represents exclusively λ_c. The rapid increase of λ in the relatively narrow temperature range $T = 0.25 - 0.45\,T_c$ is well explained by the rapid change in λ_f. In the Ginzburg-Landau region, both λ_c and λ_f are finite, with temperature independent values.[22] Experimentally the slope of $\lambda(T)$ at T_c is still an open question. In Fig. 28 the measurements have been extrapolated to T_c on the basis of measurements which extend up to $T = 0.87\,T_c$ in a field of 28.4 mT at an inclined orientation of $\mu = 25°$.[48]

In contrast to the bell-shaped curve of $\lambda(T)$ in Fig. 28, κ increases monotonously with decreasing temperature. The calculated temperature independent Ginzburg-Landau value is $\kappa/\Omega \sim 0.15$ mT · sec/rad at 25 bar.[22] The poor experimental resolution does not allow any useful comparisons with this value. However, with decreasing temperature, κ increases rapidly approaching $\kappa/\Omega \sim 2$ mT sec/rad at $0.2\,T_c$. At $0.65\,T_c$, κ undergoes a discontinuous jump from 0.3(8) in the high-temperature phase to 0.6(4) mT · sec/rad in the low-temperature phase.

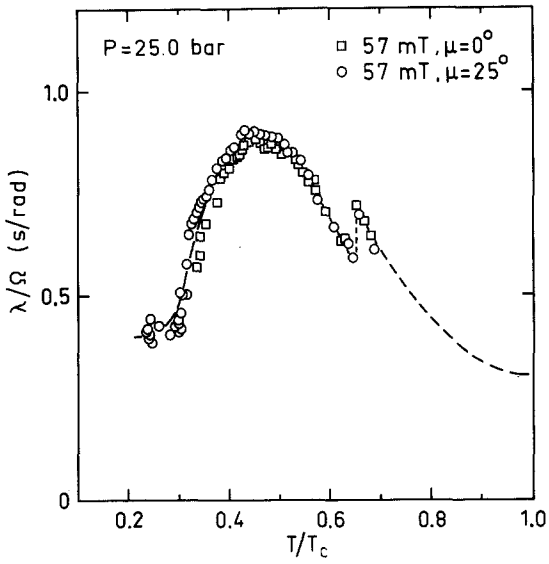

Fig. 28. The vortex susceptibility parameter λ plotted as λ/Ω vs. T/T_c: squares, the data from Fig. 27; circles, measurements in a magnetic field tilted by an angle $\mu = 25°$ with respect to the axial orientation (see Ref. 48); $P =$ 25.0 bar; $H = 56.9$ mT; $\Omega = 2.0$ rad/sec.

Finally, a second example of the analysis of the bulk-liquid-like frequency shift is shown in Fig. 29. These measurements have been performed at a low pressure of 0.5 bar where λ is large and the region suitable for the frequency shift analysis is relatively wide. The results in Fig. 29 have also been compared to a second measurement where λ is determined from the signal intensity distribution as explained in Sec. 4.3. The two sets of results are in good agreement. The value of $\lambda/\Omega = 1.69$ calculated by Thuneberg[22] agrees reasonably with the extrapolated curve (if we use the present value for $\nu_L(I)$). An estimate for the average of the experimental κ value is $\kappa/\Omega = 1.3 \pm 0.6$ mT · sec/rad in the temperature interval 0.77–$0.88T_c$. The calculated Ginzburg-Landau value is 0.37 mT · sec/rad.[22] A more comprehensive compilation of $\lambda(P, T)$ and $\kappa(P, T)$ is postponed to a forthcoming report.[48]

5. CONCLUSION

This paper presents experimental data and numerical computations on the axisymmetric textures both in the stationary and rotating states. The axially symmetric flare-out texture is in general well understood; good agreement is reached in relating experimental spectra to theoretical calcula-

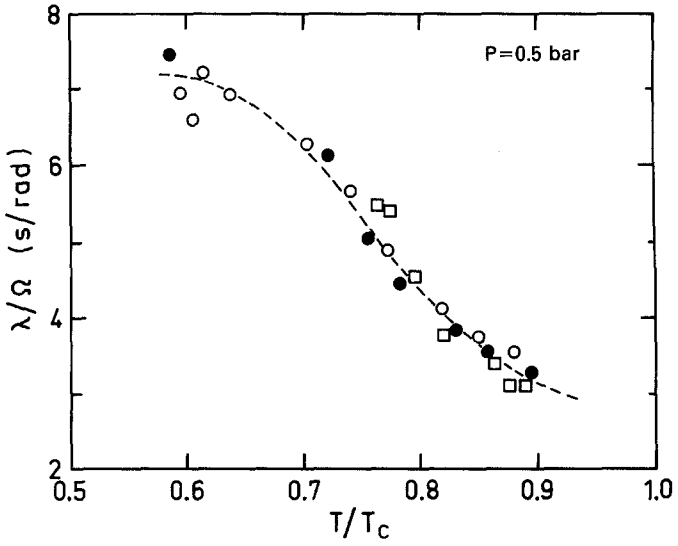

Fig. 29. Temperature dependence of λ/Ω: $P = 0.5$ bar, $H = 56.9$ mT, and $\Omega = 0.78$ rad/sec; open and filled symbols refer to forward and reverse rotation, respectively; circles, bulk-liquid-like frequency shift of the main absorption peak; squares, intensity distribution of the NMR spectrum according to the local oscillator model.

tions and pertinent textural parameters are here extracted from such comparisons. A direct fit of the measured and calculated NMR absorption as a function of frequency has not been attempted, both because of complications in the experimental techniques and in the theoretical treatment, such as, for instance, the unknown line broadening. Instead, we have used more specific features in comparing the measured cw NMR spectra to calculations. Primarily three properties of the NMR signal envelopes have been selected for this purpose:

1) the frequency spacing between the spin-wave resonance absorption peaks;
2) the overall intensity distribution under the signal envelope as compared to the expected resonance absorption according to the local oscillator picture; and finally
3) the bulk-liquid-like shift of the main resonance absorption maximum in the rotating state close to T_c.

The different methods of analysis give consistent and supplementary results, in overlapping cases good agreement prevails.

From the stationary state spectra the following textural parameters have been extracted:

1) the longitudinal resonance frequency $\nu_L(P, T)$, characteristic of ^{3}He-B, is determined from a stationary soliton-like wall defect with $\sin^2 \beta = 1$ and, when this was not available, from the high-frequency edge of the flare-out signal, corresponding to the orientation with $\sin^2 \beta = 0.8$;
2) the magnetic coherence length $\xi_H(P, T)$ is derived at pressures $P \leq 10$ bar from the intensity distribution under the signal envelope, and
3) the dipolar coherence length $\xi_D(P, T)$ is obtained at pressures $P \geq 10$ bar from the spacing of the spin-wave modes.

From the rotating state spectra, two additional parameters have been derived which control the textural free energy contributions proportional to the density of the quantized superfluid vortex lines in ^{3}He-B:

1) using all three different techniques of NMR signal analysis $\lambda(P, T)$ is determined; it contains the orienting contributions from the quantized supercurrent circulating the core and the difference in induced magnetizations inside and outside the vortex-core matter;
2) the orienting effect from the spontaneous magnetization of the core structure, described by the parameter $\kappa(P, T)$, is extracted directly from the gyromagnetic splitting of the frequency shifts of the spin-wave absorption peaks or of the main absorption maximum, when the direction of rotation is changed.

To preserve internal consistency in the data analysis, the values listed for the different textural parameters are the ones which have been derived from the analysis and then have been re-employed for extracting further parameters. Values smoothed with respect to both temperature and pressure have not been tabulated in this report. However, it is recommended that smoothed values should be worked out whenever our parameter values are used. Finally, we point out that this report will be supplemented by a forthcoming paper which contains additional data on the vortex parameters, obtained from similar measurements but at field orientations tilted with respect to the common direction of the rotation axis and the axis of cylindrical symmetry of the sample container.[48] These later measurements are analyzed by comparing the results to bulk liquid behavior, which gives good agreement with the present data analysis in axial fields, provided that ξ_H does not grow too large.

NMR on the flare-out texture has proven to be a versatile probe of superfluid ^{3}He-B: it provides both global and local information about the order-parameter distribution. The global overall features allowed us to extract useful textural lengths, while the local properties (such as the susceptibility anisotropy and the local magnetization distribution) enabled determination of the vortex parameters. The flare-out texture proves useful

also for the study of vortex-free rotational states of ^{3}He-B in the presence of normal fluid–superfluid counterflow.

ACKNOWLEDGMENTS

This report summarizes some of the NMR measurements and their analysis performed during the years 1981–1984. A large number of people have participated in this work and should rightfully be included in the list of authors, in particular Yu. M. Bunkov, I. A. Fomin, O. T. Ikkala, S. T. Islander, O. V. Lounasmaa, V. P. Mineev, H. K. Seppälä, and G. E. Volovik. We are deeply indebted to all our coworkers for their enthusiasm and relentless effort during these exciting years when the many novel features about rotating superfluid ^{3}He were discovered. This research has been supported by the Soviet Academy of Sciences and the Academy of Finland through the project ROTA.

REFERENCES

1. D. D. Osheroff, R. C. Richardson, and D. M. Lee, *Phys. Rev. Lett.* **28**, 885 (1972); D. D. Osheroff, W. J. Gully, R. C. Richardson, and D. M. Lee, *Phys. Rev. Lett.* **33**, 584 (1972).
2. P. J. Hakonen, O. T. Ikkala, S. T. Islander, and O. V. Lounasmaa, T. K. Markkula, P. Roubeau, K. M. Saloheimo, G. E. Volovik, E. L. Andronikashvili, D. I. Garibashvili, and J. S. Tsakadze, *Phys. Rev. Lett.* **48**, 1838 (1982); O. T. Ikkala, and G. E. Volovik, P. J. Hakonen, Yu. M. Bunkov, S. T. Islander, and G. A. Kharadze, *Pis'ma Zh. Eksp. Teor. Fiz.* **35**, 338 (1982) [JETP Lett. **49**, 1258 (1982)].
3. P. L. Gammel, H. E. Hall, and J. D. Reppy, *Phys. Rev. Lett.* **52**, 121 (1984); **52**, 1701 (1984).
4. P. J. Hakonen, O. T. Ikkala, S. T. Islander, O. V. Lounasmaa, and G. E. Volovik, *J. Low Temp. Phys.* **53**, 425 (1983).
5. M. Krusius, P. J. Hakonen, and J. T. Simola, *Physica* **126B**, 22 (1984).
6. Yu. M. Bun'kov, G. E. Gurgenishvili, M. Krusius, and G. A. Kharadze, *Usp. Fiz. Nauk.* **144**, 141 (1984) [*Sov. Phys.-Usp.* **27**, 731 (1984)].
7. V. P. Mineev, M. M. Salomaa, and O. V. Lounasmaa, *Nature* **324**, 333 (1986).
8. A. L. Fetter, in *Progress in Low Temperature Physics, Vol* 10, D. F. Brewer, ed. (North-Holland, New York, 1986), p. 1.
9. M. M. Salomaa and G. E. Volovik, *Rev. Mod. Phys.* **59**, 533 (1987).
10. G. A. Kharadze, in *Modern Problems in Condensed Matter Sciences*, W. P. Halperin and L. P. Pitaevskii, eds., (North-Holland, New York, to be published).
11. M. M. Salomaa and G. E. Volovik, *Phys. Rev. Lett.* **51**, 2040 (1983).
12. E. V. Thuneberg, *Phys. Rev. Lett.* **56**, 359 (1986).
13. M. M. Salomaa and G. E. Volovik, *Phys. Rev. Lett.* **56**, 363 (1986).
14. J. P. Pekola, J. T. Simola, P. J. Hakonen, M. Krusius, O. V. Lounasmaa, K. K. Nummila, G. Mamniashvili, R. E. Packard, and G. E. Volovik, *Phys. Rev. Lett.* **53**, 584 (1984).
15. H. Smith, W. F. Brinkman, and S. Engelsberg, *Phys. Rev.* **15B**, 199 (1977) and references therein.
16. A. I. Ahonen, M. Krusius, and M. A. Paalanen, *J. Low Temp. Phys.* **25**, 421 (1976).
17. D. D. Osheroff, *Physica* **90B**, 20 (1977).
18. A. D. Gongadze, G. E. Gurgenishvili, and G. A. Kharadze, *Fiz. Nizk. Temp.* **7**, 821 (1981) [*Sov. J. Low Temp. Phys.* **7**, 821 (1981)].
19. P. J. Hakonen and K. K. Nummila, *Phys. Rev. Lett.* **59**, 1006 (1987); K. K. Nummila, P. J. Hakonen, and O. Magradze, *Europhys. Lett.*, to be published.

20. M. M. Salomaa and G. E. Volovik, *Phys. Rev. B* **31**, 203 (1985).
21. P. J. Hakonen, M. Krusius, M. M. Salomaa, J. T. Simola, Yu. M. Bunkov, V. P. Mineev, and G. E. Volovik, *Phys. Rev. Lett.* **51**, 1362 (1983).
22. E. V. Thuneberg, *Phys. Rev. B* **36**, 3583 (1987).
23. K. Maki and M. Nakahara, *Phys. Rev. B* **27**, 4181 (1983).
24. P. J. Hakonen and G. E. Volovik, *J. Phys. C* **15**, L1277 (1982).
25. K. W. Jacobsen and H. Smith, *J. Low Temp. Phys.* **52**, 527 (1983).
26. W. F. Brinkman, H. Smith, D. D. Osheroff, and E. I. Blount, *Phys. Rev. Lett.* **33**, 624 (1974).
27. D. D. Osheroff, S. Engelsberg, W. F. Brinkman, and L. R. Corruccini, *Phys. Rev. Lett.* **34**, 190 (1975).
28. A. I. Ahonen, T. A. Alvesalo, M. T. Haikala, M. Krusius, and M. A. Paalanen, *J. Phys. C* **8**, L269 (1975).
29. P. J. Hakonen, O. T. Ikkala, S. T. Islander, T. K. Markkula, P. M. Roubeau, K. M. Saloheimo, D. I. Garibashvili, and J. S. Tsakadze, *Cryogenics* **23**, 243 (1983).
30. P. J. Hakonen, M. Krusius, and H. K. Seppälä, *J. Low Temp. Phys.* **60**, 187 (1985).
31. K. Maki and P. Kumar, *Phys. Rev. B* **16**, 4805 (1977).
32. D. D. Osheroff, in *Quantum Fluids and Solids*, S. D. Trickey, E. D. Adams, and J. W. Dufty, eds., (Plenum Press, New York, 1977), p. 161.
33. D. D. Osheroff, *Phys. Rev. Lett.* **33**, 1009 (1974).
34. A. J. Leggett, *Rev. Mod. Phys.* **47**, 331 (1975).
35. R. A. Webb, R. E. Sager, and J. C. Wheatley, *Phys. Rev. Lett.* **35**, 615 (1975).
36. J. W. Serene and D. Rainer, *Physics Reports* **101**, 221 (1983).
37. T. A. Alvesalo, T. Haavasoja, and M. T. Manninen, *J. Low Temp Phys.* **45**, 373 (1981).
38. E. K. Zeise, J. Saunders, A. I. Ahonen, C. N. Archie, and R. C. Richardson, *Physica* **108B**, 1213 (1981).
39. D. S. Greywall, *Phys. Rev. B* **33**, 7520 (1986); **27**, 2747 (1983).
40. M. A. Paalanen, M. C. Cross, W. O. Sprenger, W. van Roosbroeck, and D. D. Osheroff, *J. Low Temp. Phys.* **34**, 607 (1979).
41. G. F. Spencer and G. G. Ihas, *Phys. Rev. Lett.* **48**, 1118 (1982).
42. W. F. Brinkman and M. C. Cross, in *Progress in Low Temperature Physics, Vol. 7a*, D. F. Brewer, ed. (North-Holland, Amsterdam, 1978), p. 127.
43. J. W. Serene and D. Rainer, in *Quantum Fluids and Solids*, S. B. Trickey, E. D. Adams, and J. W. Dufty, eds. (Plenum, New York, 1977), p. 112.
44. J. C. Wheatley, *Rev. Mod. Phys.* **47**, 415 (1975).
45. J. A. Sauls and J. W. Serene, *Phys. Rev. B* **24**, 183 (1981).
46. D. F. Brewer, D. S. Betts, A. Sachrajda, and W. S. Truscott, *Physica* **108B**, 1059 (1981).
47. D. Candela, N. Masuhara, D. S. Sherrill, and D. O. Edwards, *J. Low Temp. Phys.* **63**, 369 (1986).
48. P. J. Hakonen, M. Krusius, and J. T. Simola, *J. Low Temp. Phys.*, to be published.